Search for supersymmetry in diphoton final states with the CMS detector

Matthew Lawrence Joyce

June 14, 2021

CONTENTS

1. The Standard Model of Particle Physics . . . 7
- 1.1 The Standard Model . . . 7
- 1.2 Electroweak Symmetry Breaking . . . 8
- 1.3 Problems with the SM . . . 13

2. Supersymmetry . . . 15

3. The Large Hadron Collider . . . 16
- 3.1 Introduction . . . 16
- 3.2 Injection Complex . . . 16
- 3.3 Tunnel and Magnets . . . 17
- 3.4 Luminosity . . . 17

4. Compact Muon Solenoid . . . 24
- 4.1 Introduction . . . 24
- 4.2 Coordinate System . . . 25
- 4.3 Tracker . . . 26
  - 4.3.1 Pixel Detector . . . 27
  - 4.3.2 Strip Detector . . . 28
- 4.4 Electromagnetic Calorimeter . . . 29
  - 4.4.1 Crystals . . . 29
  - 4.4.2 Barrel and Endcaps . . . 30
  - 4.4.3 Preshower layer . . . 31
  - 4.4.4 Performance . . . 31
- 4.5 Hadronic Calorimeter . . . 32
- 4.6 Superconducting Solenoid . . . 33
- 4.7 Muon System . . . 34

5. MIP Timing Detector (MTD) . . . 38
- 5.1 Introduction . . . 38
- 5.2 Barrel Timing Layer . . . 40
  - 5.2.1 LYSO:Ce crystals . . . 41

5.2.2 SiPMs . . . 41
5.2.3 Glue qualification . . . 41

6. CMS Trigger System . . . 43
6.1 L1 trigger . . . 43
6.1.1 Calorimeter trigger . . . 43
6.1.2 Muon trigger . . . 45
6.1.3 Global Trigger . . . 45
6.2 High Level Trigger . . . 45
6.3 Trigger efficiency . . . 46

7. CMS Particle and Event Reconstruction . . . 47
7.1 Tracks . . . 47
7.2 Calorimeter clusters . . . 48
7.3 Object identification . . . 48
7.3.1 Muons . . . 48
7.3.2 Electrons . . . 49
7.3.3 Photons . . . 50
7.3.4 Jets . . . 51
7.4 Missing transverse momentum . . . 51

8. Data Analysis . . . 52
8.1 Overview . . . 52
8.2 Data . . . 52
8.3 Monte Carlo samples . . . 53
8.4 Object definitions . . . 53
8.4.1 Photons . . . 54
8.4.2 Electrons . . . 55
8.4.3 Muons . . . 55
8.5 Backgrounds . . . 55
8.5.1 Instrumental background . . . 55
8.5.2 Electroweak background . . . 57
8.5.3 Irreducible background . . . 57

LIST OF FIGURES

1.1 Illustration of the Higgs potential for $\mu^2 < 0$ 12
1.2 Summary of content of the SM. 14

3.1 LHC interaction points 19
3.2 Layout of LHC accelerator complex [17]. 20
3.3 Proton bunch capture onto RF bucket [7]. 21
3.4 Cross section of LHC dipole [10] 22
3.5 Integrated luminosity delivered by the LHC to the CMS experiment each year from 2010-2018. 23

4.1 Schematic of CMS detector [24] 25
4.2 Transverse slice of the CMS detector[8]. 26
4.3 Cross section (side) of CMS tracker prior to the Phase 1 upgrade during the year-end technical stop of 2016/2017. Each line represents a detector module while double lines indicate back-to-back strip modules. Surrounding the pixel tracker (PIXEL) is the strip detector, which is divided into the Tracker Inner Barrel (TIB), Tracker Outer Barrel (TOB), Tracker Inner Disks (TID), and Tracker Endcaps (TEC). Reprinted from Reference [13]. 27
4.4 Cross section (side) of pixel detector. The lower half , labeled ”Current”, shows the design prior to 2017 while the upper half, labeled ”Upgrade”, shows the design after the upgrade. Reprinted from Resource [12] 28
4.5 $PbWO_4$ crystals. Left: EB crystal with APD. Right: EE crystal with VPT. Reprinted from [14] 30
4.6 Schematic of ECAL. Reprint from [14] 32
4.7 Longitudinal view of HCAL [2] 34
4.8 Longitudinal slice of CMS detector while operating at 3.8-T central magnetic field. The right-hand side of the figure shows a mapping of the magnetic field lines while the left-hand side shows a mapping of the field strength. Reprint from [11] . . . 35

4.9 Cross-section of one quadrant of the CMS detector. The DTs are labeled as "MB" (Muon Barrel) and the CSCs are labelled as "ME" (Muon Endcap). The RPCs are "RB" for those in the barrel and "RE" for those in the endcap. Reprint from [25]. 36

5.1 Timeline for LHC 38
5.2 Vertices from a simulated 200 pileup event with MTD timing resolution of $\sim$30 ps. The red dots represent the simulated vertices while the yellow lines indicate vertices reconstructed without the use of timing information. The black crosses and blue open circles represent tracks and vertices reconstructed using time information from the MTD. Reprint from 39
5.3 Schematic view of MTD 40
5.4 Overview of the BTL 42
5.5 Readout unit for the BTL. 42

6.1 L1 trigger system. Reprint from [3] 44

7.1 The Bremsstrahlung photons continue along a straight trajectory while the electron path is bent by the magnetic field. This results in energy deposited in the calorimeter for such electrons to be spread out along the ϕ-direction. 50

8.1 Two examples of GGM supersymmetry breaking processes resulting in final states conaining two photons and missing transverse momentum. The T5gg model (left) shows gluinos produced from $p-p$ collisions which subsequently result in two neutralinos, each decaying to a photon and a gravitino. The T6gg model (right) shows squarks produced from $p-p$ collisions following a similar decay chain. 52
8.2 Mismeasurement of Jet3 results in an inbalance in the events transverse momentum. 56

LIST OF TABLES

1.1 Boson fields in the SM 8
1.2 Fermions in the SM. The first two numbers listed in the third column give the supermultiplet representation under $SU(3)_C$ and $SU(2)_L$ respectively. A **1** means that it is not charged under that group and therefore will not couple to the associated force. A **3** as the first number means that it has color charge and couples to the strong force. A **2** for the second number means that it has weak isospin and couples to the weak force. The third number gives the value of the weak isospin. Adjoint representation is specified by the presence of a bar over the number. 9

4.1 Summary of signals expected for each particle type in each sub-detector. 24

6.1 Primary HLT 46

8.1 Data Samples 53
8.2 Summary of loose ID photons cuts 54
8.3 Summary of $Z\gamma\gamma \to \nu\nu\gamma\gamma$ model validation 58

1. THE STANDARD MODEL OF PARTICLE PHYSICS

1.1 The Standard Model

The Standard Model (SM) of particle physics is a Lorentz-invariant quantum field theory (QFT) that describes the dynamics of elementary particles. Three critical developments leading to the formation of the SM, as described by Steven Weinberg[26], were the quark model proposed by Gell-Mann[19] and Zweig[29] in 1964, the idea of gauge symmetry by Yang and Mills[28] in 1954, and the notion of spontaneous symmetry breaking proposed by Goldstone[20] in 1961. This ultimately led to the SM in its current form as a non-Abelian gauge theory with the symmetry group

$$G_{SM} = SU(3)_C \otimes SU(2)_L \otimes U(1)_Y \tag{1.1}$$

where $SU(3)_C$ is responsible for strong interactions and $SU(2)_L \otimes U(1)_Y$ is responsible for unified electromagnetic and weak interactions, also known as electroweak interactions.

Associated with each of these symmetry groups is a set of massless spin-1 vector fields called gauge bosons. These are listed in Table 1.1 along with the associated charge or generator for that group. There are eight such gauge bosons in $SU(3)_C$ called gluons $G_\mu^{1,\dots,8}$. There are three gauge bosons $W_\mu^{1,2,3}$ in $SU(2)_L$ and one gauge boson B_μ in $U(1)_Y$. The gauge bosons mediate the interactions between spin-1/2 fields ψ called fermions. At this point it's worth noting that the W and B gauge fields are not observable bosons, but are mixed by electroweak symmestry breaking to produce observable bosons. The details of this will be covered in Section 1.2.

There are twelve fermion fields which can be split into six lepton fields and six quark fields. Both quarks and leptons are comprised of three generations. For quarks there are three "up-type" quarks (up u, charm c, and top t) and three "down-type" quarks (down d, strange s, and bottom b). The lepton fields are electron e, muon μ, tau τ, and three neutrino fields ν_e, ν_μ, and ν_τ. The fermion fields and their representations under G_{SM} are listed in Table 1.2. Each fermion field can be expressed in terms of left and right chirality fields, which are represented by a doublets ψ_L in the left-handed case and singlets ψ_R in the right-handed case with

$$\psi = \psi_R + \psi_L \tag{1.2}$$
$$\psi_R = \frac{1}{2}(1+\gamma^5)\psi \tag{1.3}$$
$$\psi_L = \frac{1}{2}(1-\gamma^5)\psi \tag{1.4}$$

The SM also contains a complex scalar doublet field ϕ called the Higgs field in honor of Peter Higgs, who was among one of the physicists who proposed its existence in 1964 [21].

Tab. 1.1: Boson fields in the SM

Symbol	Associated Charge	Symmetry group
B_μ	weak hypercharge Y	$U(1)_Y$
$G_\mu^{1,\ldots,8}$	color $C = (r, g, b)$	$SU(3)_C$
$W_\mu^{1,2,3}$	weak isospin T_3	$SU(2)_L$

The strong interaction is described by the theory of quantum chromodynamics (QCD). The Lagrangian for the QCD interaction can be written as

$$\mathcal{L}_{QCD} = \bar{\psi}(i\gamma^\mu D_\mu - m)\psi - \frac{1}{2}TrG_{\mu\nu}G^{\mu\nu} \tag{1.5}$$

where

$$G_{\mu\nu} = \partial_\mu G_\nu - \partial_\nu G_\mu - ig_s[G_\mu, G_\nu] \tag{1.6}$$
$$D_\mu = \partial_\mu - ig_s G_\mu \tag{1.7}$$

g_s is related to the strong coupling constant, and m is the fermion mass, which in this case must be a quark since they are the only fermions with color charge.

1.2 Electroweak Symmetry Breaking

A crucial feature of the SM is electroweak symmetry breaking. The electroweak interaction, first proposed by Glashow, Weinberg, and Salam in the 60's, is the unified description of electromagnetic and weak interactions under the $SU(2)_L \otimes U(1)_Y$ symmetry. The electromagnetic interaction is described by quantum electrodynamics (QED), which is an Abelian gauge

Tab. 1.2: Fermions in the SM. The first two numbers listed in the third column give the supermultiplet representation under $SU(3)_C$ and $SU(2)_L$ respectively. A **1** means that it is not charged under that group and therefore will not couple to the associated force. A **3** as the first number means that it has color charge and couples to the strong force. A **2** for the second number means that it has weak isospin and couples to the weak force. The third number gives the value of the weak isospin. Adjoint representation is specified by the presence of a bar over the number.

Name	Notation	Representation under $SU(3)_C \otimes SU(2)_L \otimes U(1)_Y$
Left-handed quark doublet	$\begin{pmatrix} u_L \\ d_L \end{pmatrix}, \begin{pmatrix} c_L \\ s_L \end{pmatrix}, \begin{pmatrix} t_L \\ b_L \end{pmatrix}$	$(3,\ 2,\ \frac{1}{6})$
Right-handed up-type quark singlet	$u_R^\dagger,\ c_R^\dagger,\ b_R^\dagger$	$(\bar{3},\ 1,\ \text{-}\frac{2}{3})$
Right-handed down-type quark singlet	$d_R^\dagger,\ s_R^\dagger,\ t_R^\dagger$	$(\bar{3},\ 1,\ \frac{1}{3})$
Left-handed lepton doublet	$\begin{pmatrix} \nu_{eL} \\ e_L \end{pmatrix}, \begin{pmatrix} \nu_{\mu L} \\ \mu_L \end{pmatrix}, \begin{pmatrix} \nu_{\tau L} \\ \tau_L \end{pmatrix}$	$(1,\ 2,\ \text{-}\frac{1}{2})$
Right-handed charged lepton singlet	$e_R^\dagger,\ \mu_R^\dagger,\ \tau_R^\dagger$	$(\bar{1},\ 1,\ 1)$

theory under the $U(1)_{EM}$ symmetry group. The gauge boson in QED is the photon and couples to electric charge Q. The QED Lagrangian is given by

$$\mathcal{L}_{QED} = \bar{\psi}(i\gamma^{\mu} D_{\mu} - m)\psi - \frac{1}{4} F_{\mu\nu} F^{\mu\nu} \tag{1.8}$$

32 where

$$F_{\mu\nu} = \partial_{\mu} A_{\nu} - \partial_{\nu} A_{\mu} \tag{1.9}$$

$$D_{\mu} = \partial_{\mu} + ieQA_{\mu} \tag{1.10}$$

33 and A_{μ} is the electromagnetic or photon field.

The Lagrangian for the unbroken $SU(2)_L \otimes U(1)_Y$ symmetry is given by

$$\mathcal{L}_{EW} = \bar{\psi} i\gamma^{\mu} D_{\mu}\psi - Tr\frac{1}{8} W_{\mu\nu} W^{\mu\nu} - \frac{1}{4} B_{\mu\nu} B^{\mu\nu} \tag{1.11}$$

34 where

$$W_{\mu\nu} = \partial_{\mu} W_{\nu} - \partial_{\nu} W_{\mu} - ig_w [W_{\mu}, W_{\nu}] \tag{1.12}$$

$$B_{\mu\nu} = \partial_{\mu} B_{\nu} - \partial_{\nu} B_{\mu} \tag{1.13}$$

with a separate fermion term for each field ψ_R and ψ_L. The covariant derivative D_{μ} is given by

$$D_{\mu} = \partial_{\mu} + ig_w T_i W_{\mu}^i + ig_Y \frac{Y}{2} B_{\mu} \tag{1.14}$$

35 with W_{μ}^i and T_i written in terms of raising and lowering operators

$$W_{\mu}^{\pm} = \frac{1}{\sqrt{2}}(W_{\mu}^1 \mp W_{\mu}^2) \tag{1.15}$$

$$T^{\pm} = \frac{1}{\sqrt{2}}(T_1 \pm T_2) \tag{1.16}$$

$$W_{\mu}^0 = W_{\mu}^3 \tag{1.17}$$

$$T^0 = T_3 \tag{1.18}$$

The neutral portion of the covariant derivative $ig_w T_3 W_{\mu}^3 + ig_Y \frac{Y}{2} B_{\mu}$must contain the electromagnetic term $ieAQ$ for the electromagnetic interaction to be unified with the weak interaction, so the W_{μ}^3 and B_{μ} fields need to linear combinations of the photon field A_{μ} and another field Z_{μ}. This relationship can be written in terms of the electroweak mixing angle θ_w, also known as the Weinberg angle, as

$$\begin{pmatrix} A_{\mu} \\ Z_{\mu} \end{pmatrix} = \begin{pmatrix} \cos\theta_W & \sin\theta_W \\ -\sin\theta_W & \cos\theta_W \end{pmatrix} \begin{pmatrix} B_{\mu} \\ W_{\mu}^3 \end{pmatrix} \tag{1.19}$$

The weak isospin T_3 and weak hypercharge Y can be related to the electric charge Q with the Gell-Mann-Nishijima formula

$$Y = 2(Q - T_3) \tag{1.20}$$

36 and the coupling constants g_w, g_Y, and e are related to the mixing angle by

$$e = g_w \cos\theta_W = g_Y \sin\theta_W \tag{1.21}$$

$$\sin\theta_W = \frac{g_Y}{\sqrt{g_w^2 + g_Y^2}} \tag{1.22}$$

$$\cos\theta_W = \frac{g_w}{\sqrt{g_w^2 + g_Y^2}} \tag{1.23}$$

At this point the $W_\mu^{1,2,3}$ and B_μ fields have been mixed to produce the observable fields W_μ^+, W_μ^-, A_μ, and Z_μ, but this is still inconsistent with experimental observations as these bosons and all of the fermions are still massless in this model. In order to generate the masses while maintaining the renormalizability of the gauge theory the symmetry needs to be spontaneously broken. This is done by the introduction of a complex scalar doublet field called the Higgs field which is expressed as

$$\phi = \begin{pmatrix} \phi^+ \\ \phi^0 \end{pmatrix} = \frac{1}{\sqrt{2}} \begin{pmatrix} \phi_1 + i\phi_2 \\ \phi_3 + i\phi_4 \end{pmatrix} \tag{1.24}$$

where the fields ϕ_i are real scalar fields. The Lagrangian for the Higgs field is

$$\mathcal{L}_{Hiigs} = (D_\nu\phi)^\dagger(D^\nu\phi) - V(\phi^\dagger\phi) \tag{1.25}$$

with the potential $V(\phi^\dagger\phi)$ being given by

$$V(\phi^\dagger\phi) = \mu^2\phi^\dagger\phi + |\lambda|(\phi^\dagger\phi)^2 \tag{1.26}$$

and the covariant derivative

$$D_\nu = \partial_\nu - \frac{i}{2}g_w W_\nu^i \sigma_i - \frac{i}{2}g_Y B_\nu \tag{1.27}$$

Since $\mu^2 < 0$, this potential has the shape of a sombrero as is shown in Figure 1.1. The scalar fields have some positive vacuum expectation value (VEV) satisfying

$$\phi^\dagger\phi = v = \sqrt{-\frac{\mu^2}{\lambda}} \tag{1.28}$$

at the minimum which allows us to write the ground state as

$$\phi_{ground} =< 0|\phi|0 >= \frac{1}{\sqrt{2}} \begin{pmatrix} 0 \\ v \end{pmatrix} \tag{1.29}$$

Expanding the Higgs field about it's minimum as

$$\phi_{ground} \rightarrow \phi(x) = \frac{1}{\sqrt{2}} e^{i\sigma_\alpha \theta^\alpha(x)} \begin{pmatrix} 0 \\ v + h(x) \end{pmatrix}, \alpha = 1, 2, 3 \tag{1.30}$$

results in a massive field $h(x)$ and and three massless scalar fields, or Goldstone bosons, $\theta_{1,2,3}$ which represent degrees of freedom. By then transforming into the unitary gauge we can remove the phase factor, thereby eliminating the explicit appearance of the three Goldstone bosons in the Lagrangian. In gauging away the Goldstone bosons, the three degrees of freedom reappear as longitudinal polarization states of the W^+, W^-, and Z bosons. In other words, the W and Z bosons have become massive by "eating" the Goldstone bosons.

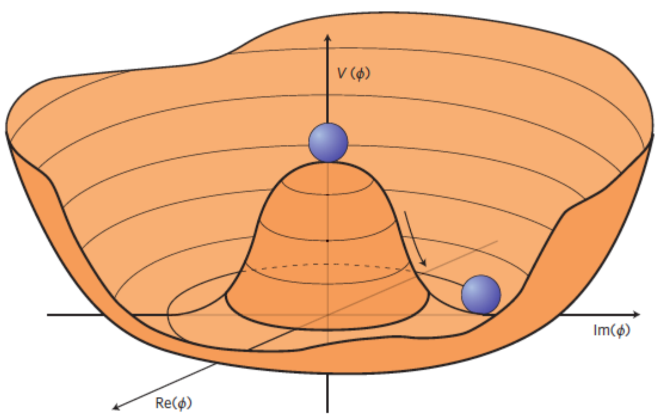

Fig. 1.1: The Higgs potential is shown as a function of the complex scalar field's real and imaginary parts. The balls illustrate that the stable vacuum state of nature is not located at $\phi = 0$ because the symmetry at that point is spontaneously broken. Instead the stable vacuum state of nature is located somewhere along the circle of minimum potential. Reprint from [5]

Writing the Lagrangian in Equation 1.25 in terms of the physical W and

Z fields and evaluating at the VEV gives

$$\begin{aligned}\mathcal{L}_{Higgs} =& \frac{1}{2}\partial_\nu h \partial^\nu h + \frac{1}{4} g_w^2 W_\nu^+ W^{-\nu}(v+h)^2 \\ &+ \frac{1}{8}\frac{g_w^2}{\cos^2\theta_W} Z_\nu Z^\nu (v+h)^2 - V[\frac{1}{2}(v+h)^2]\end{aligned} \tag{1.31}$$

The v^2 terms give the W and Z boson masses and the h^2 term gives the mass of the Higgs boson as

$$M_W = \frac{1}{2} g_w v \tag{1.32}$$

$$M_Z = \frac{1}{2} v \frac{g_w}{\cos\theta_W} = \frac{M_W}{\cos\theta_W} \tag{1.33}$$

$$M_H = \sqrt{2}|\mu| \tag{1.34}$$

while the photon remains massless.

At this point we can summarize the particle content of the SM and their allowed interactions in a way that is seen in Figure 1.2.

1.3 Problems with the SM

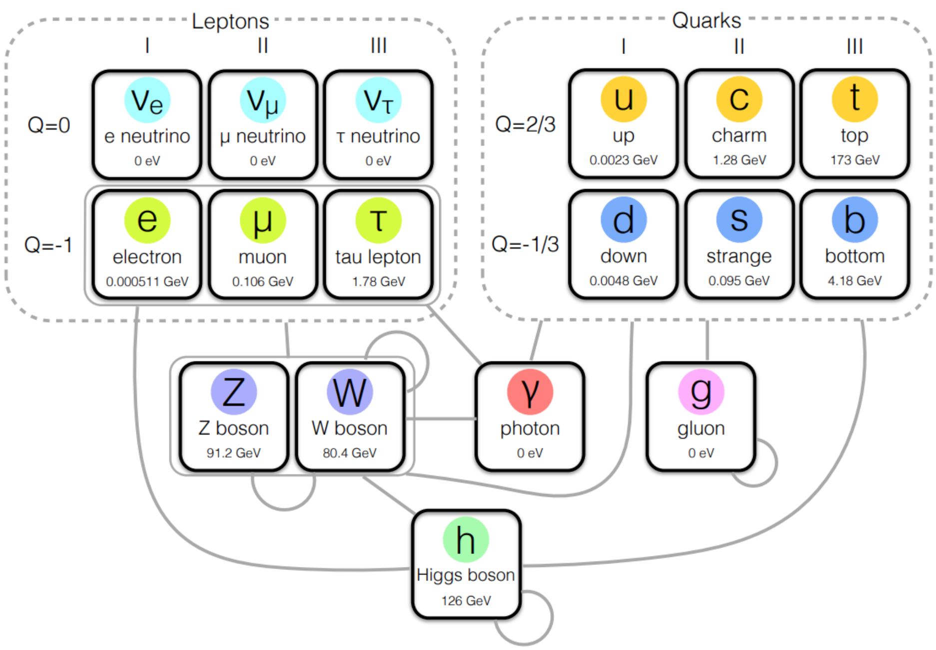

Fig. 1.2: Summary of particle content in the SM. Gray lines connecting groups of particles indicates allowed interactions. Self-coupling is indicated by a gray line connecting a particle to itself. The leptons and quarks are organized in columns corresponding to generation, which is specified at top, and rows corresponding to electric charge Q, which is listed to the left. Each particle's mass is listed beneath its name and symbol. It should be noted that neutrinos in the SM are still treated as massless leptons despite the fact that experimental evidence has established that at least two of the neutrinos are massive. Reprinted from [22]

51

2. SUPERSYMMETRY

3. THE LARGE HADRON COLLIDER

3.1 Introduction

The Large Hadron Collider (LHC) is a 26.7 kilometer-long, two-ring particle accelerator and collider located on the border of France and Switzerland at the European Organization for Nuclear Research (CERN). During normal operations the LHC maintains two counter-rotating beams of proton bunches that collide at four interaction points (IP) with up to $\sqrt{s} = 14$ TeV center of mass energy and a luminosity of $10^{34}\text{cm}^{-2}\text{s}^{-1}$. The ALICE (Point 2), ATLAS (Point 1), CMS (Point 5), and LHC-b experiments each have a detector at one of these interaction points as scene in Figure 3.1 . The CMS and ATLAS are general-purpose detectors while LHC-b specializes in beauty quark studies. ALICE is a heavy-ion experiment which uses $^{208}Pb - p$ or $^{208}Pb -^{208} Pb$ collisions that can also be produced by the LHC.

3.2 Injection Complex

In order to bring the protons from rest up to their target collision energy a series of accelerators, as shown in Figure 3.2, are used. The acceleration sequence begins with the injection of hydrogen gas into a duoplasmatron. Here a bombardment of electrons ionize the hydrogen atoms while an electric field pushes them through the duoplasmatron cavity. The result is 100 keV protons being passed on to a quadrapole magnet which guides them into the aperture of a linear accelerator (LINAC2). The radio frequency (RF) cavities in LINAC2 accelerate the protons up to 50 MeV. At this point the protons are sent into one of four rings in the Proton Synchrotron Booster (PSB). The PSB repeatedly accelerates the protons around a circular path until they reach an energy of 1.4 GeV. The bunches of protons from each PSB ring are then sequentially injected into the single-ringed Proton Synchrotron (PS). Each bunch injected into the PS are captured by one of the ”buckets” (Figure 3.3) provided by the PS RF system which also manipulates the bunches into the desired profile and proton density. These proton bunches are accelerated to 25 GeV and injected into the Super Proton Synchrotron

(SPS) where they are accelerated to 450 GeV. Finally the proton bunches are injected into the LHC ring where they are accelerated to 6.5 TeV and collided in 25 ns intervals to yield a center of mass energy of $\sqrt{s} = 13$ TeV.

3.3 Tunnel and Magnets

The LHC was designed to produce collisions with up to $\sqrt{s} = 14$ TeV. That requires confining and guiding 7 TeV protons around the circumference of the LHC ring. The ring is housed in a 4 meter-wide underground tunnel that ranges in depth between 45 and 170 meters below the surface. This tunnel was repurposed from the Large Electron-Positron (LEP) Collider which previously occupied the space. For this reason the tunnel is not completely circular but is instead made up of alternating curved and straight sections of 2500 m and 530 m in length respectively. The straight sections, labeled 1-8 in Figure 3.1, are used as either experimental facilities or sites for hardware necessary for LHC operations such as RF cavities for momentum cleaning, quadrupole magnets for beam focusing, and sextupole magnets for acceleration and betatron cleaning.

Steering a 7 TeV proton beam around the curved sections requires a magnetic field of 8.33 Tesla which is provided by 1223 superconducting dipole magnets cooled to 1.9 K. A cross section of the LHC dipole is shown in Figure 3.4. Supercooled liquid helium flows through the heat exchanger pipe to cool the iron yolk to a temperature of 1.9 K. Ultra high vacuum is maintainted in the outer volume to provide a layer of thermal insulation between the inner volume and the outer steel casing. Inside the iron yolk is a twin bore assembly of niobium-titanium superconducting coils. Two parallel beam pipes are located within the focus of the superconducting coils. This is the ultra high vacuum region where the subatomic particles are confined as they travel around the LHC ring.

3.4 Luminosity

The number of events generated per second for specific process having cross-section σ_{event} is given by:

$$\frac{dN_{event}}{dt} = L\sigma_{event} \tag{3.1}$$

where L in the machine luminosity. The machine luminosity for a Gaussian beam distribution can be written in terms of the beam parameters as:

$$L = \frac{N_b^2 n_b f_{rev} \gamma_r}{4\pi \epsilon_n \beta *} F \tag{3.2}$$

where N_b is particle density in each bunch, n_b is the number of bunches in each beam, f_{rev} is the frequency of revolution, and γ_r is the relativistic gamma factor. The variables ϵ_n and $\beta*$ are the normalized transverse beam emittance and the beta function at the IP respectively, while F is the geometric reduction factor depending due to the beams' crossing angle at the IP. [17]

The total number of events produced over a given amount of time would then be

$$N_{event} = \sigma_{event} \int L dt = \sigma_{event} L_{integrated}. \tag{3.3}$$

The integrated luminosity delivered each year to the CMS experiment is shown in 3.5. The analysis presented here uses data collected from the 2016, 2017, and 2018 campaigns which gives a combined integrated luminosity of 158.7 fb^{-1}.

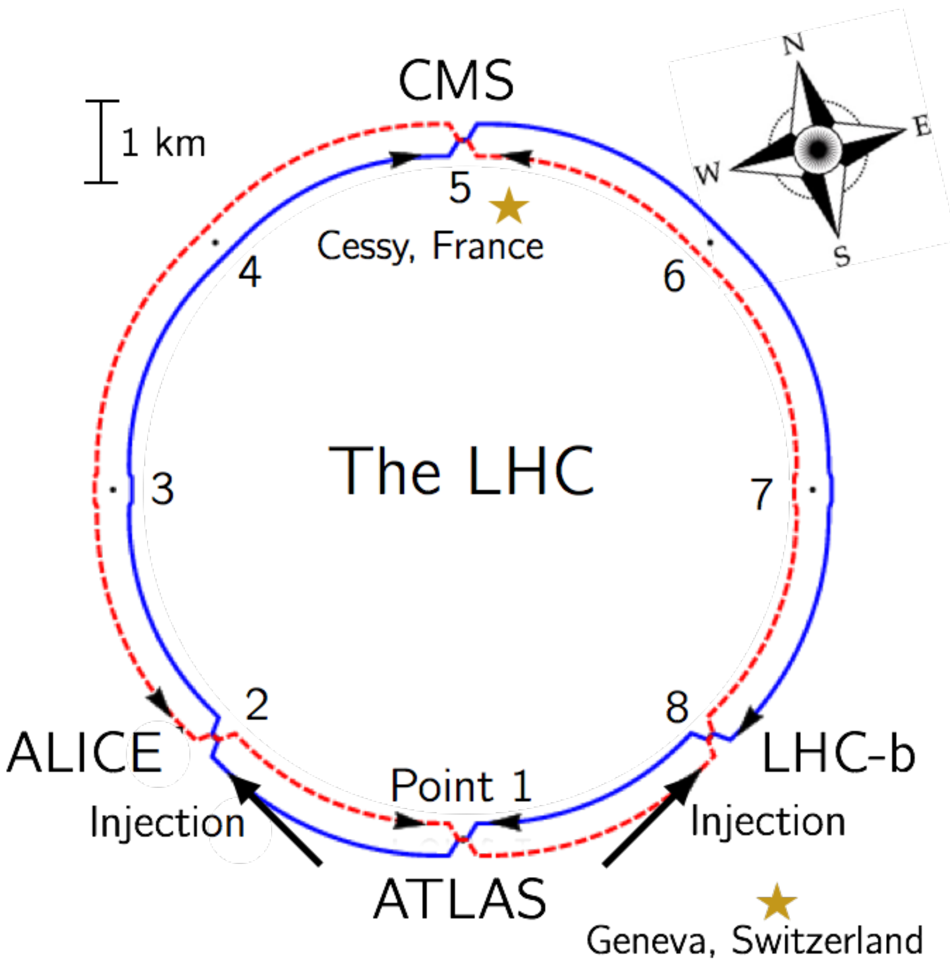

Fig. 3.1: Interaction points of the LHC

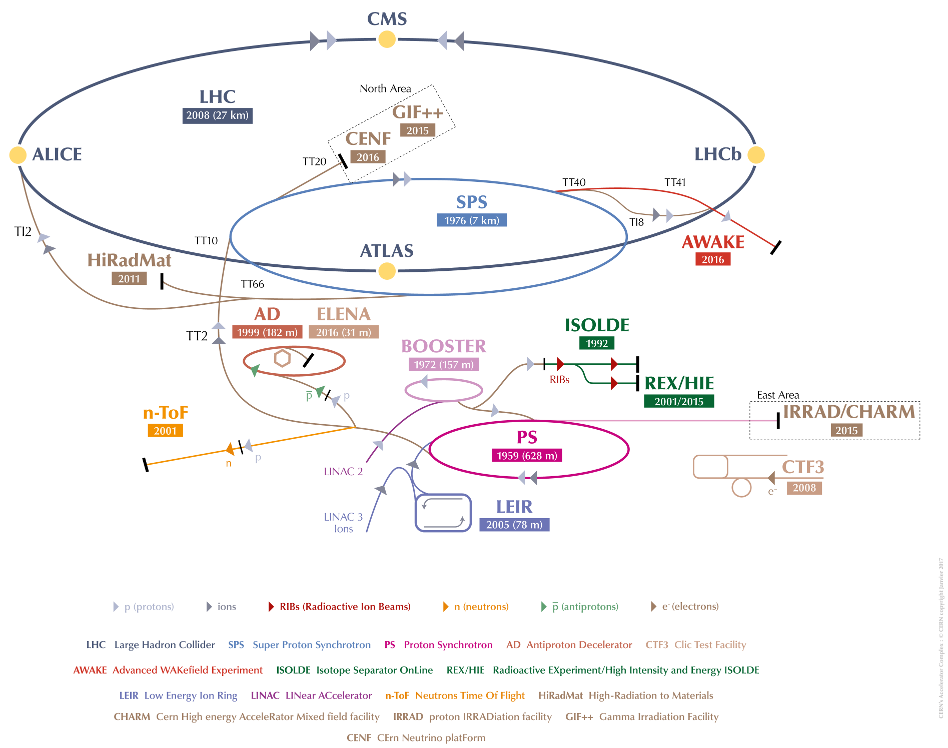

Fig. 3.2: Layout of LHC accelerator complex [17].

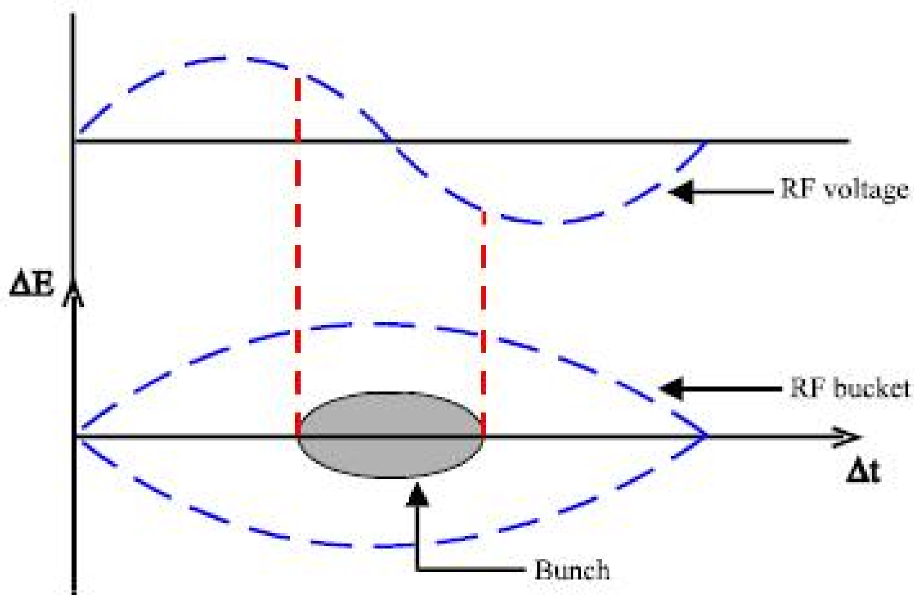

Fig. 3.3: Proton bunch capture onto RF bucket [7].

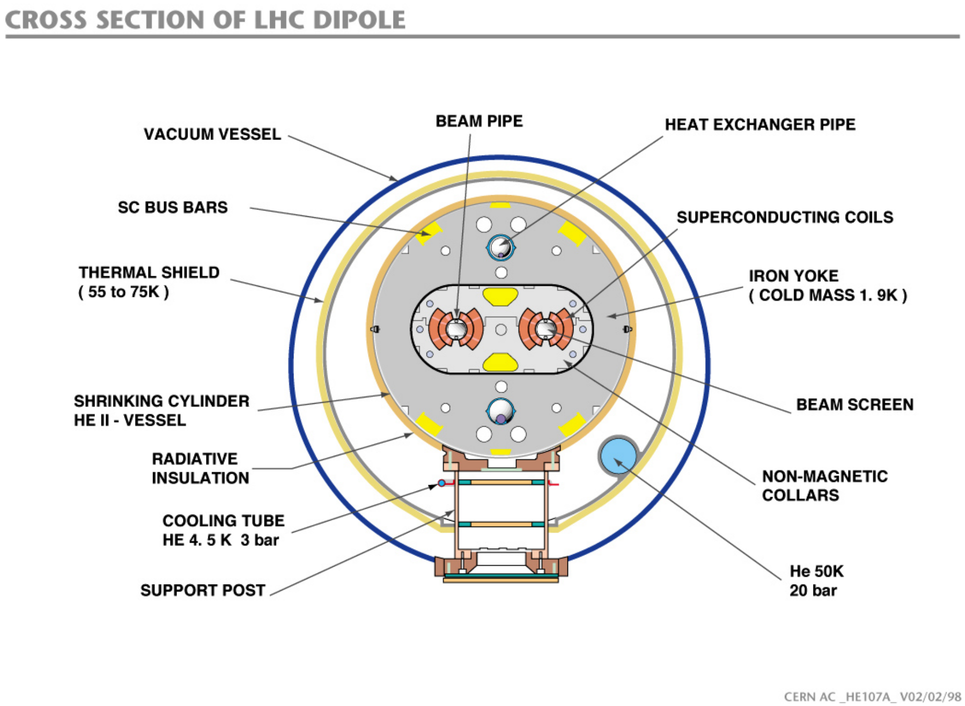

Fig. 3.4: Cross section of LHC dipole [10]

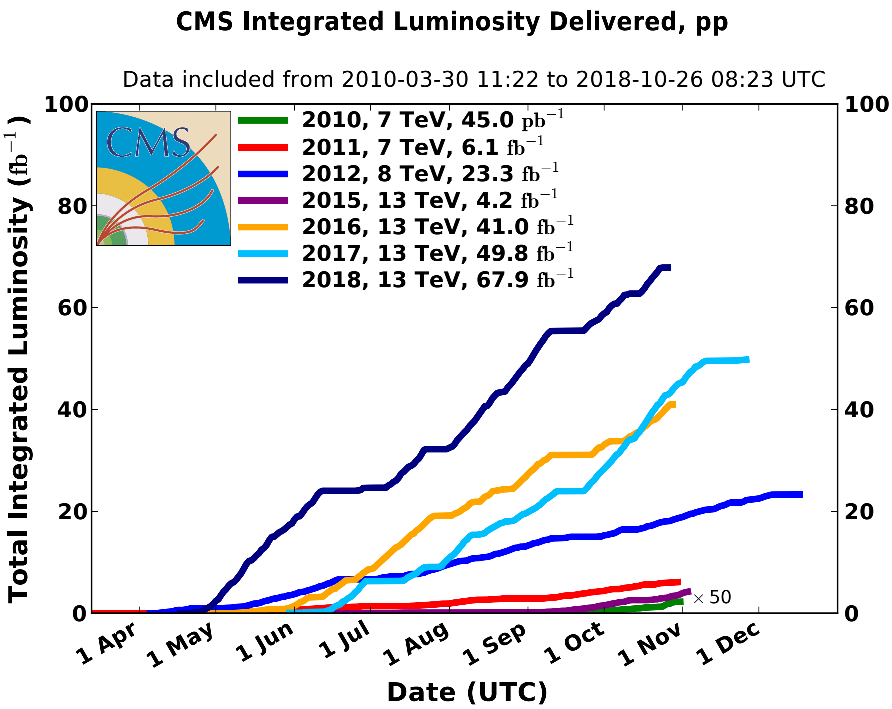

Fig. 3.5: Integrated luminosity delivered by the LHC to the CMS experiment each year from 2010-2018.

4. COMPACT MUON SOLENOID

4.1 Introduction

About 100 meters below the town of Cessy, France at Point 5 is the Compact Muon Solenoid (CMS). The CMS is a general purpose detector weighing 14,000 tonnes with a length of 28.7 meters and a 15.0-meter diameter that was designed to accurately measure the energy and momentum of particles produced in the proton-proton or heavy-ion collisions at the LHC [14]. A perspective view of of the detector is shown in Figure 4.1. In order to get a full picture of what is being produced by the collisions the CMS detector must be able identify the resulting particles as well as accurately measure their energy and momentum. For this reason the detector was designed to be a collection of specialized sub-detectors, each of which contributes data used in the reconstruction of a collision.

At the heart of the CMS detector is a 3.8-Tesla magnetic field produced by a superconducting solenoid. Inside the 6-meter diameter solenoid are three layers of sub-detectors. These make up the inner detector and are, in order from innermost to outermost, the silicon tracker, the electromagnetic calorimeter (ECAL), and the hadronic calorimeter (HCAL). Outside the solenoid is the muon system. A transverse slice of the detector (Figure 4.2) shows the sub-detectors and how different types of particles interact with with them. Table 4.1 shows a summary of which sub-detectors are expected to produce signals for different types of particles.

Particle	Tracker	ECAL	HCAL	Muon
Photons	No	Yes	No	No
Electrons	Yes	Yes	No	No
Hadrons (charged)	Yes	Yes	Yes	No
Hadrons (neutral)	No	No	Yes	No
Muons	Yes	Yes	Yes	Yes
Invisible (ν, SUSY, etc)	No	No	No	No

Tab. 4.1: Summary of signals expected for each particle type in each sub-detector.

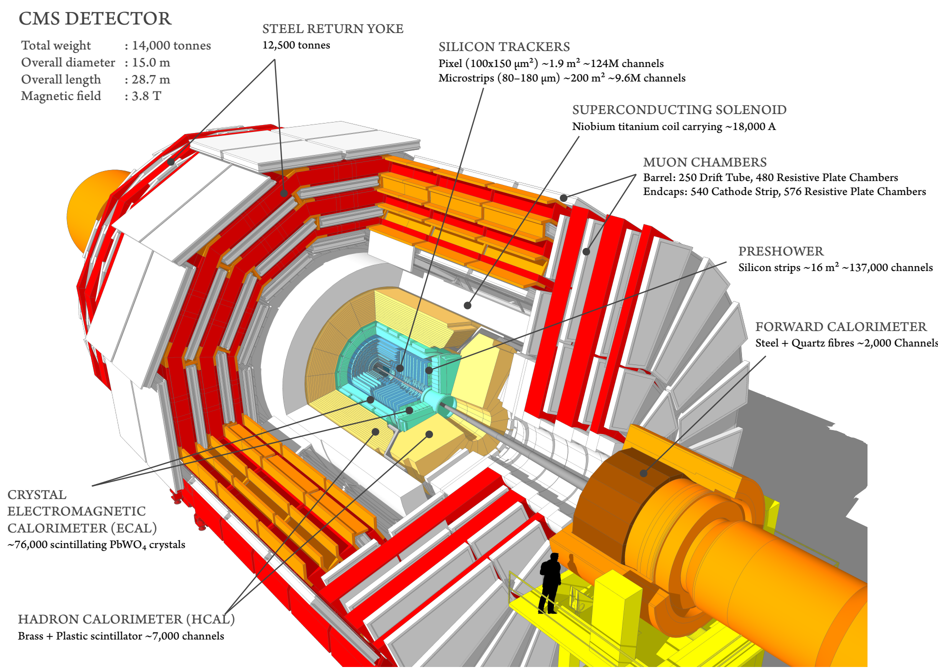

Fig. 4.1: Schematic of CMS detector [24]

142 ## *4.2 Coordinate System*

The origin of the coordinate system used by CMS is centered at the nominal collision point in the center of the detector. A right-handed Cartesian system is used with the x-axis pointing radially inward toward the center of the LHC ring, y-axis pointing vertically upward, and the z-axis pointing tangent to the LHC ring in the counterclockwise direction as viewed from above. CMS also uses an approximately Lorentz invariant spherical coordinate system spanned by three basis vectors. They are the transverse momentum p_T, pseudorapidity η, and azimuthal angle ϕ. The transverse momentum and azimuthal angle translate to the Cartesian system in the following ways using the x and y-components of the linear momentum:

$$p_T = \sqrt{(p_x)^2 + (p_y)^2} \tag{4.1}$$

$$\phi = tan^{-1}\frac{p_y}{p_x} \tag{4.2}$$

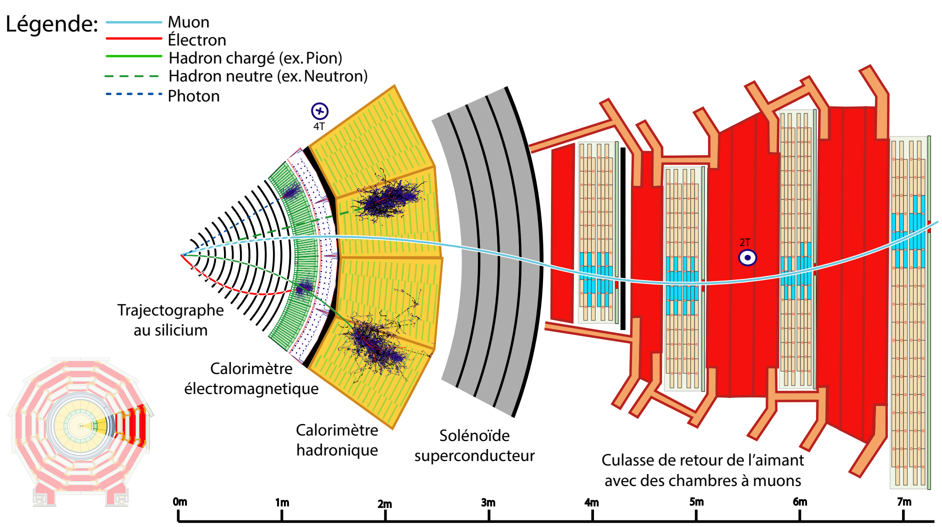

Fig. 4.2: Transverse slice of the CMS detector[8].

while the pseudorapidity can be translated using the polar angle θ relative the positive z-axis as

$$\eta = -ln[tan\frac{\theta}{2}]. \tag{4.3}$$

4.3 Tracker

The innermost sub-detector in CMS is the silicon tracker. The tracker is used to reconstruct tracks and vertices of charged particles. In order to give precise reconstruction of charged particle trajectories it needs to be position as close as possible to the IP and have high granularity. The close proximity to the IP requires the materials to be tolerant to the high levels of radiation in that region. Being the innermost sub-detector it must also minimally disturb particles as they pass through it into the other sub-detectors. These criteria led to the design of the tracker using silicon semiconductors.

The silicon tracker is made up of two subsystems, an inner pixel detector and an outer strip tracker which are oriented in a cylindrical shape with an overall diameter of 2.4 m and length of 5.6 m centered on the interaction point. Both subsystems consist of barrel and endcap regions which can be seen in Figure 4.3.

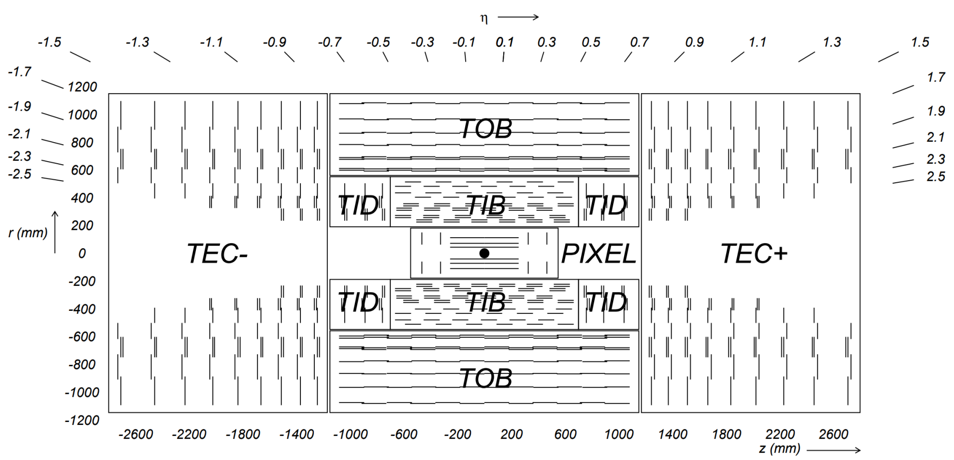

Fig. 4.3: Cross section (side) of CMS tracker prior to the Phase 1 upgrade during the year-end technical stop of 2016/2017. Each line represents a detector module while double lines indicate back-to-back strip modules. Surrounding the pixel tracker (PIXEL) is the strip detector, which is divided into the Tracker Inner Barrel (TIB), Tracker Outer Barrel (TOB), Tracker Inner Disks (TID), and Tracker Endcaps (TEC). Reprinted from Reference [13].

4.3.1 Pixel Detector

The pixel detector is the innermost subsystem in the silicon tracker and spans the pseudorapidity range $|\eta| < 2.5$ and is responsible for small impact parameter resolution which is important for accurate reconstruction of secondary vertices [14]. In order to produce these precise measurements a very high granularity is required. In addition to this the proximity to the IP means that one expects there to be high occupancy of the tracker. These constraints are met by using pixels with a cell size of 100 x 150 μm^2.

The original pixel detector was designed for operation at the nominal instantaneous luminosity of 10^{34} cm^{-2}s^{-1} with 25 ns between proton bunch crossings, resulting in on average about 25 proton-proton interactions occurring per bunch crossing or pileup [13]. During the LHC technical shutdown of 2016/17, the pixel detector underwent the scheduled Phase 1 upgrade which would allow operation at higher levels of instantaneous luminosity and pileup. Figure 4.4 shows a cross sectional view in the r-z plane. Prior to 2017 there were three barrel layers and two endcap layers on each side which provide three very precise space points for each charged particle. The upgrade decreased the radius of the innermost barrel layer from 4.4 cm to

3.0 cm and added a fourth barrel layer as well as adding third endcap layer to each side. Each of the endcap layers consisted of two half-disks populated with pixel modules whereas the upgraded endcap layers were split into inner and outer rings. [12]

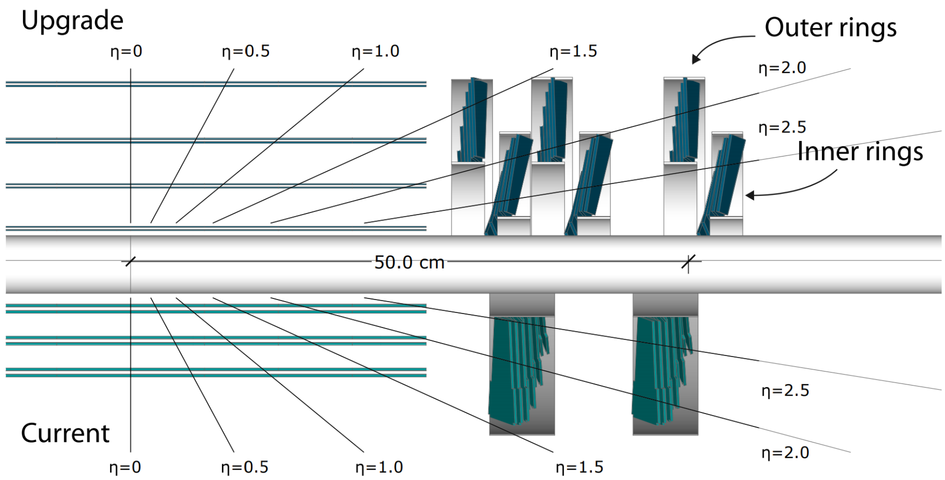

Fig. 4.4: Cross section (side) of pixel detector. The lower half , labeled ”Current”, shows the design prior to 2017 while the upper half, labeled ”Upgrade”, shows the design after the upgrade. Reprinted from Resource [12]

4.3.2 Strip Detector

The silicon strip detector surrounds the pixel detector and is comprised of four subsystems, the Tracker Inner Barrel (TIB), the Tracker Outer Barrel (TOB), the Tracker Inner Disks (TID), and the Tracker Endcaps (TEC), all of which can be seen in Figure 4.3 [14]. The TIB and TID both use 320 μm thick silicon micro-strip sensors oriented along z and r respectively. The TIB has four layers while the TID is composed of three layers. This geometry allows the TIB and TID to combine to provide up to four $r - \phi$ measurements on charged particle trajectories.

Surrounding the TIB and TID is the TOB, which extends between $z \pm 118$ cm. This subsystem consists of six layers of 500 μm thick silicon micro-strip sensors with strip pitches ranging from 122 μm to 183 μm, providing six more $r - \phi$ measurements in addition to those from the TIB/TID subsystems. Beyond the z range of the TOB is the TEC. Each TEC is made up of nine disks. Each of the nine disks has up to seven concentric rings of micro-strip sensors oriented in radial strips with those on the inner four rings being 320 μm thick and the rest being 500 μm thick, providing up to nine ϕ measurements for the trajectory of a charged particle.

To provide additional measurements of the z coordinate in the barrel and r coordinate in the disks a second micro-strip detector module is mounted back-to-back with stereo angle 100 mrad in the first two layers of the TIB and TOB, the first two rings of the TID, and rings 1, 2, and 5 of the TEC. The resulting single point resolution is 230 μm in the TIB and 530 μm in the TOB. The layout of these subsystems ensures at least nine hits for $|\eta| < 2.4$ with at least four of hits yielding a 2D measurement.

4.4 Electromagnetic Calorimeter

The electromagnetic calorimeter (ECAL) lies just outside the tracker and is a hermetic homogeneous calorimeter designed to measure the energy deposited by electrons and photons. It consists of a central barrel (EB) with 61200 lead tungstate ($PbWO_4$) crystals which is closed by two endcaps (EE), each having 7324 crystals. Highly-relativistic charged particles passing through a crystal primarily lose energy by producing bremsstrahlung photons. Photons lose energy by producing $e^- - e^+$ pairs. In front of each EE is a preshower (ES) detector which acts as a two-layered sampling calorimeter. The crystals in the EB are instrumented with avalanche photodiodes (APDs) while the EE crystals are instrumented with vacuum phototriodes (VPTs). The ECAL design was strongly driven to be sensitive to the di-photon decay channel of the Higgs boson. This led to the design of a calorimeter that was fast, radiation-hard, and had good spatial and energy resolution.

4.4.1 Crystals

In order to provide a good spacial resolution it was necessary for the ECAL to have a fine granularity. The small Molier radius (22 mm) and short radiation length (8.9 mm) of $PbWO_4$ allows for fine granularity while maintaining good energy resolution by containing nearly all of the energy from an EM shower without the need for a restrictively thick crystal layer. The $PbWO_4$ scintillation is also fast enough that approximately 80 percent of an EM shower is produced within 25 ns, which is the also the amount of time between bunch crossings at the LHC. These crystals have a Gaussian-shaped spectrum spanning from 360 nm to 570 nm with a maximum at approximately 440 nm. While $PbWO_4$ is relatively radiation-hard, the amount of ionizing radiation seen by the crystal leading up to the HL-LHC era of operations causes wavelength-dependent degradation in light transmission. The scintillation mechanism however is unchanged so this damage can be tracked and accounted for by injecting laser light near the peak wavelength of the emission spectrum into the crystals to monitor optical transparency.

Light produced in the crystal is transmitted along its length and collected at the rear by either an APD in the EB or a VPT in one of the EE. Light output is temperature dependent so the crystals are kept at precisely 18°C at which the yield is about 4.5 photoelectrons per MeV. The EB and EB crystals, which have a tuncated pyramidal shape to match the lateral development of the shower, along with their photosensors are shown in Figure 4.5.

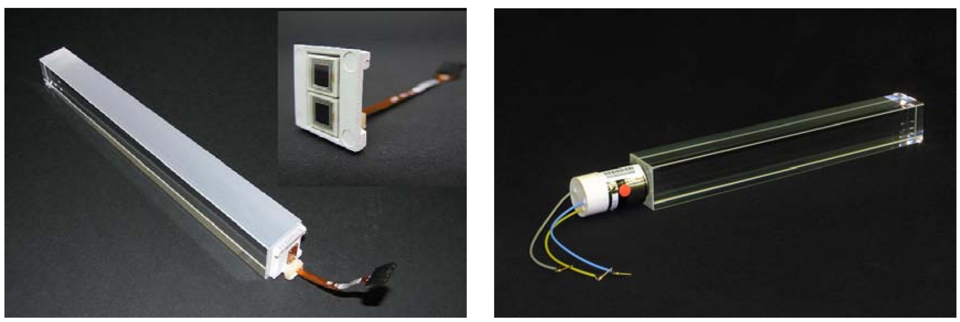

Fig. 4.5: $PbWO_4$ crystals. Left: EB crystal with APD. Right: EE crystal with VPT. Reprinted from [14]

4.4.2 Barrel and Endcaps

The EB covers the pseudorapidity range $|\eta| < 1.479$ and uses crystals that are 230 mm long, which corresponds to 25.8 radiation lengths. The front face of each crystal measures 22×22 mm^2 while the rear face measures 26×26 mm^2. These are grouped in 36 supermodules (SM), each comprised of 1700 crystals arranged in a 20×85 grid in $\phi \times \eta$. Each SM spans half the length of the barrel and covers 20° in ϕ. On the back face of each crystal is a pair of APDs (semiconductor diodes). APDs are compact, immune to the longitudinal 3.8 T magnetic field produced by the solenoid at this location, and resistant to the radiation levels expected in the EB over a ten year period. They also have high enough gain to counter to low light yield of the crystals. All of this makes them an ideal choice for use in the EB. Each APD has an active area of 5×5 mm^2 and are operated at a gain of 50 which requires a bias voltage between 340 and 430 V. As the gain of the APDs is highly dependent on the applied bias voltage and any gain instability would translate to degradation in energy resolution, very stable power supplies are used to maintain voltages within a few tens of mV.

The EE cover the pseudorapidity range $1.497 < |\eta| < 3.0$. The crystals in the EE have a 28.62×28.62 mm^2 front face cross section and 30×30 mm^2 rear face cross section. Each crystal is 220 mm long which corresponds to 24.7 radiation lengths and are grouped in 5×5 units called supercrystals (SCs). Two halves, called *Dees*, make up each EE. Each Dee contains 138 SCs and 18 partial SCs which lie along the inner and outer circumference. On the back of each crystal in EE is a VPT which is a conventional photomultiplier with a single gain stage. While not as compact as the APDs used in the EB, the VPTs are a more suitable for the more hostile environment at higher η. Each VPT has a 25-mm diameter and approximately 280 mm^2 of active area. Though the VPT gain and quantum efficiency are lower than that of the APDs this is offset by the larger active area allowing for better light collection. Figure 4.6 shows the orientation of the crystals, modules, and supermodules within the ECAL. [14]

4.4.3 Preshower layer

In front of each EE is a preshower (ES) detector. The main purpose of the ES is to identify photons resulting from $\pi^0 \rightarrow \gamma\gamma$ within the pseudorapidity range $1.653 < |\eta| < 2.6$, but it also aids in the identification of electrons against minimum ionizing particles (MIPs) and provides a spacial resolution of 2 mm compared to the 3 mm resolution of the EB and EE. The ES acts as a two-layered sampling calorimeter. Lead radiators make up the first layer. These initiate electromagnetic showers from incoming electrons or photons. The deposited energy and transverse profiles of these showers are then measured by the silicon strip sensors which make up the second layer.

4.4.4 Performance

The energy resolution of the ECAL can be parameterized as

$$\frac{\sigma}{E} = \frac{S}{\sqrt{E}} \oplus \frac{N}{E} \oplus C \tag{4.4}$$

where S is the stochastic term characterizing the size of photostatistical fluctuations, N is the term characterizing the contributions of electronic, digital, and pileup noise, and C is a constant which accounts for crystal performance non-uniformity, intercalibration errors, and leakage of energy

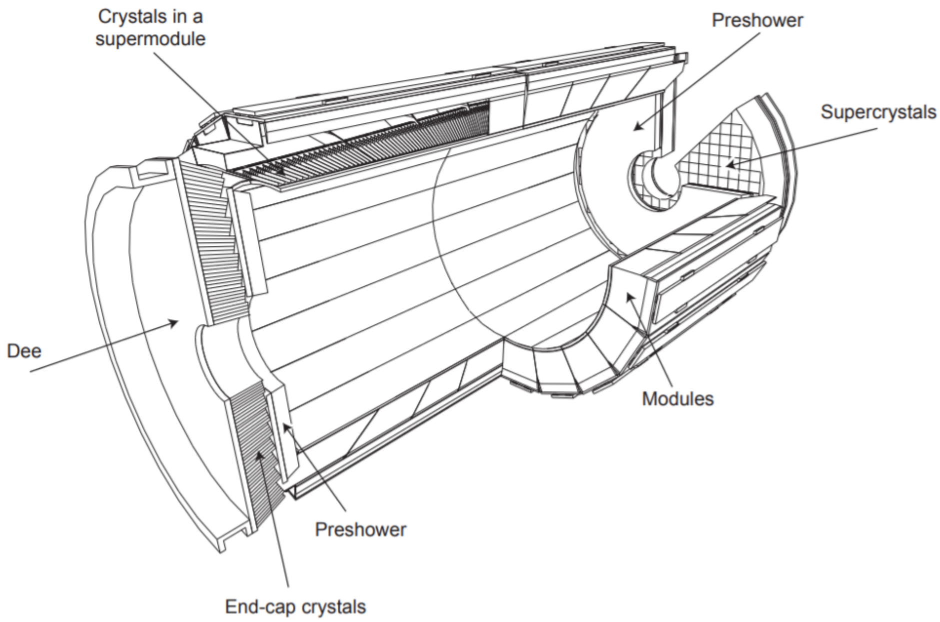

Fig. 4.6: Schematic of ECAL. Reprint from [14]

from the back of a crystal. The values for these terms, as measured in a beam test using 20 to 250 GeV electrons, are $S = 0.028$ GeV$^{1/2}$, $N = 0.12$ GeV, and $C = 0.003$. [14]

4.5 Hadronic Calorimeter

In the space between the bore of the superconducting magnet and the ECAL is the Hadronic Calorimeter (HCAL) [2]. The HCAL is a sampling calorimeter used for the measurement of hadronic jets and apparent missing transverse energy resulting from neutrinos or exotic particles. It is made up of alternating layers of plastic scintillator tiles and brass absorbers. EM showers are generated by charged/neutral hadrons in the brass absorber. Charged particles in the shower then produce scintillation light in the plastic scintillator. Wavelength-shifting optical fibers embedded in the scintillator collect and guide the scintillation light to pixelated hybrid photodiodes. A longitudinal cross-section view in Figure 4.7 shows the geometric layout of the HCAL's barrel (HB), outer barrel (HO), endcap (HE), and forward (HF) sections. The HB is comprised of 17 scintillator layers extending from 1.77 to 1.95 m and covers the pseudorapidity range of $|\eta| < 1.4$. The HO lies outside the solenoid and is composed of only scintillating material. This increases the interaction depth of the calorimeter system to a minimum of $11\lambda_I$ for $|\eta| < 1.26$ and thus reduces energy leakage. Also located inside the solenoid are the two HE which cover pseudorapidities $1.3 < |\eta| < 3.0$ and provide a thickness of $10\lambda_I$. In the forward region is the HF. This is located 11.2 m away from the IP and covers the $2.9 < |\eta| < 5.2$. As the HF is exposed to the highest levels of particle flux, it uses quartz fibers embedded in steel absorbers rather than the materials used in the other parts of the HCAL. Showers initiated by the absorbers produce Cerenkov light in the quartz which transmits along to the fibers to photomultiplier tubes (PMTs).

The HCAL inherently has lower energy resolution than the ECAL. A large portion of the energy from hadronic showers is deposited in the absorbers and never makes it to the scintillation material. There are also the possibilities that showers can be initiated prior to the particles reaching HCAL or a charged particle could deposit energy in the ECAL through bremsstrahlung. The combined energy resolution of the ECAL and the HCAL barrels can be parameterized as

$$\frac{\sigma}{E} = \frac{S}{\sqrt{E}} \oplus C, \tag{4.5}$$

where E is the energy of the incident particle. Theses quantities were measured in a beam test using 2 to 350 GeV/c hadrons, electrons, and muons. The stochastic term is $S = 0.847\ \mathrm{GeV}^{1/2}$, and the constant term is $C = 0.074$ [4].

4.6 Superconducting Solenoid

In between the HCAL barrel and outer barrel is the superconducting solenoid magnet. The magnet is 12 m long with a 6-m inner diameter and provides the bending power necessary to precisely measure the momentum of charged particles. While it is capable of producing a 4 T magnetic field, the magnet is typically operated at 3.8 T. This is done to prolong the lifetime of the magnet. The Niobium Titanium coils used to create the uniform 3.8-T magnetic field are suspended in a vacuum crystat and cooled by liquid helium to a temperature of 4.5 K. The magnet has a stored energy or 2.6 GJ when operating at full current. There are five wheels in the barrel and three disks on each endcap that make up a 12,000 ton steel yoke which serves to return the magnetic flux. This, along with a mapping of the calculated field

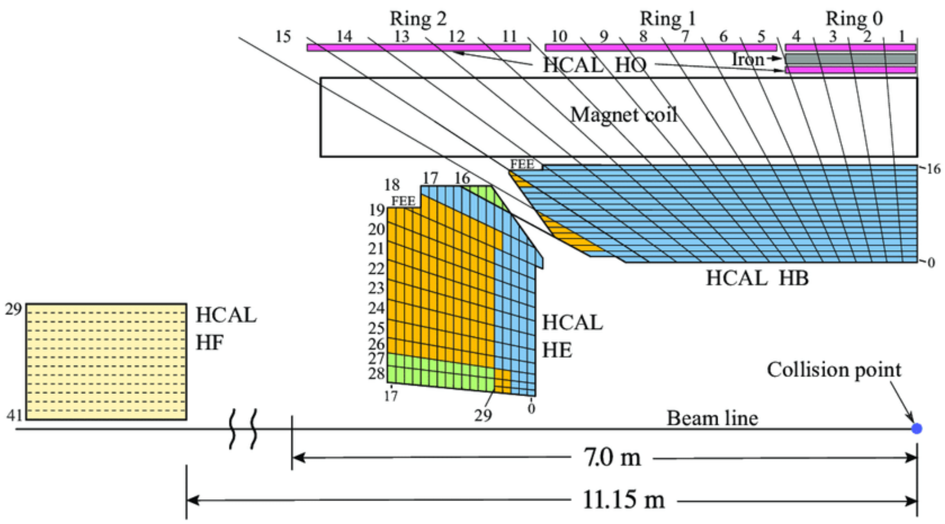

Fig. 4.7: Longitudinal view of HCAL [2]

strength, can be seen in Figure 4.8. More details on the superconducting solenoid magnet can be found at [1]

4.7 Muon System

Embedded in magnet return yoke and encapsulating all of the other subdetectors is the muon system. The muon system is the outermost layer because muons don't interact via the strong force and electromagnetic interactions alone are not enough stop them due to their large mass, therefore the only particles that are capable of making it to the muon system are muons and weakly-interacting particles such as neutrinos. The muon system is comprised of three different types of detectors. These are drift tube (DT) chambers, cathode strip chambers (CSC), and resistive plate chambers (RPC). A cross-sectional view of the muon system along with the rest of the CMS detector is shown in Figure 4.9.

The DT chambers are used barrel region for $|\eta| < 1.2$. Each chamber is comprised of three superlayers which are made up of four staggered layers of rectangular drift cells. Each of these drift cells contains a mixture of Ar and CO_2 gases. An anode wire, located at the center of each tube, is made of gold-plated stainless steel and is held at 3.6 kV. The gas is ionized when a charged particle passes through and the resulting free electrons are attracted to the anode wire. As these electrons pass through the gas they

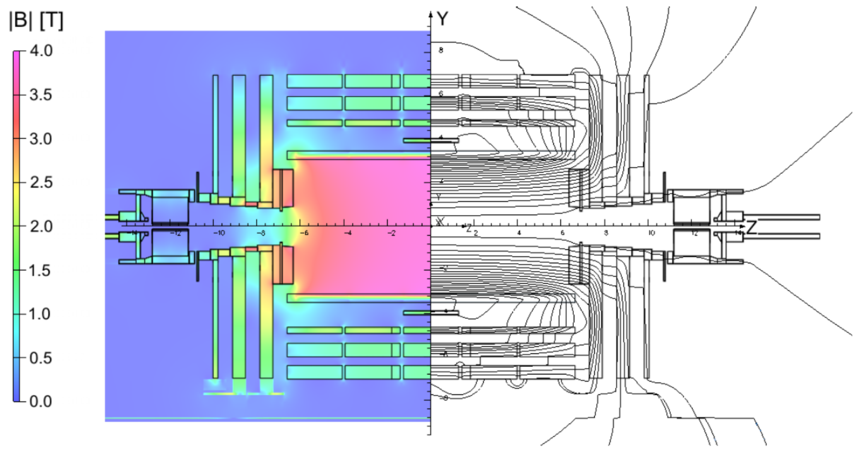

Fig. 4.8: Longitudinal slice of CMS detector while operating at 3.8-T central magnetic field. The right-hand side of the figure shows a mapping of the magnetic field lines while the left-hand side shows a mapping of the field strength. Reprint from [11]

cause further ionization which results in an electron avalanche. The layers of drift cells are oriented in such a way that two of the three superlayers give the muon position in the ϕ-direction and one gives the position in the z-direction. The result is a spacial resolution of 77-123 μm along the ϕ direction and 133-193 μm along the z direction for each DT chamber [15].

On the endcaps, covering the pseudorapidity range of $0.9 < |\eta| < 2.4$, are the CSCs. In this region there is a higher muon flux as well non-uniform magnetic fields so this portion of the muon system must have higher granularity provided by the CSCs. Each of these chambers contain panels that divide it into six staggered layers. The cathode strips are oriented along the r-direction to give position measurements in the ϕ-direction while anode wires run perpendicular in between the panels to give r-direction position measurements. The spacial resolution provided by the CSCs is 45-143 μm [25].

Both the endcap and barrel regions, spanning $|\eta| < 1.6$, contain RPCs to provide more precise timing measurements. Each RPC is a gaseous parallel-plate detector. High voltage is applied to two large plates which have a layer of gas between them. Outside the chamber is an array of cathode strips which is used to detect electron cascades resulting from muons passing through and ionizing the gas. Where the DTs and CSCs provide precise position information, the RPCs have a very fast response time which gives

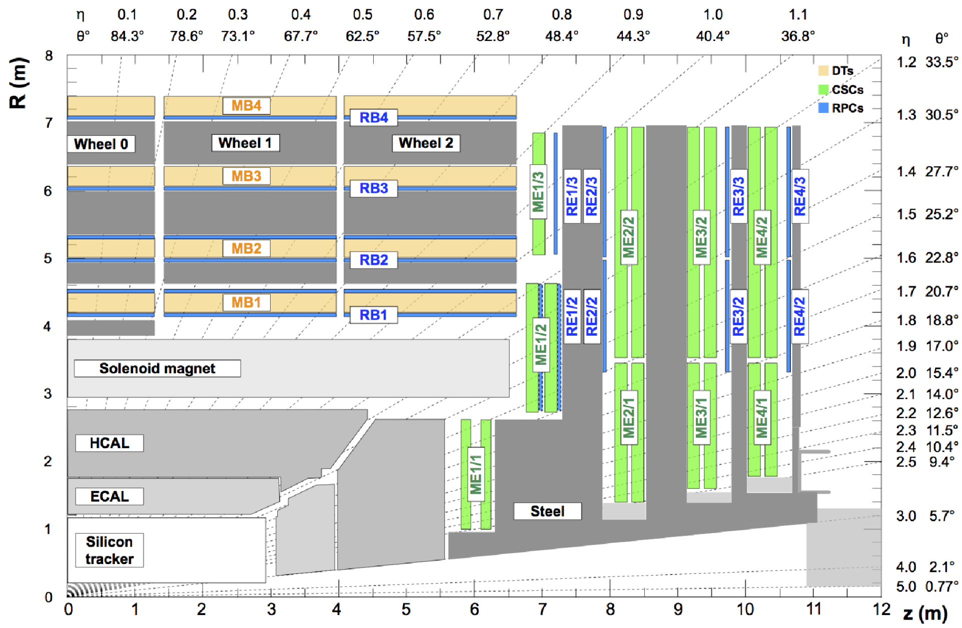

Fig. 4.9: Cross-section of one quadrant of the CMS detector. The DTs are labeled as "MB" (Muon Barrel) and the CSCs are labelled as "ME" (Muon Endcap). The RPCs are "RB" for those in the barrel and "RE" for those in the endcap. Reprint from [25].

a time resolution better than 3 ns [25]. This allows for the RPCs to be used as a dedicated muon trigger that can insure each muon is assigned to the correct bunch crossing.

5. MIP TIMING DETECTOR (MTD)

5.1 Introduction

In the coming years the LHC will be working toward upgrades that will lead a substantial increase in luminosity. The timeline for future operations of the LHC is shown in Figure 5.1. In 2019 the LHC entered a two-year shutdown, Long Shutdown 2 (LS2). Upgrades of the LHC injector complex to increase the beam brightness will take place during this shutdown. After LS2 the LHC will enter Run 3 which will run for three years at 13-14 TeV. At the completion of Run 3 the LHC will enter Long Shutdown 3 (LS3) which will last approximately 2.5 years. During LS3 the optics in the interaction region will be upgraded to produce smaller beams at the interaction point. The completion of this upgrade will usher in the High Luminosity (HL-LHC) era or Phase 2 of LHC operations, during which the combination of brighter beams and a new focusing scheme at the IP allows for a potential luminosity of 2x10^{35} $cm^{-2}s^{-1}$ at the beginning of each fill [6].

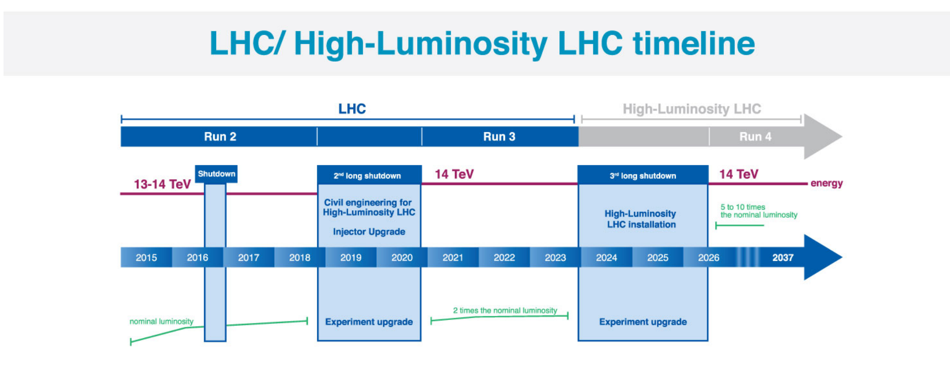

Fig. 5.1: Timeline for LHC [16]

The increased luminosity results in more interactions per bunch crossing or pileup. In order to limit the amount of pileup the experiments must disentangle to more manageable levels, the nominal scenario would be operating at a stable luminosity of 5.0×10^{34} cm^{-2} s^{-1}. This would limit the pileup to an average of 140. The ultimate scenario for operations would be running at 7.5×10^{34} cm^{-2} s^{-1} which brings the average pileup up to 200. The CMS detector in its current state is not capable of dealing with ≈140-200 pileup. At this level of pileup the spacial overlaps of tracks and energy depositions would lead to a degradation in the ability to identify and reconstruct hard interactions. In order to preserve the data quality of the current CMS detector this increased pileup must be reduced to an equivalent level approximately equal to current LHC operations which is ∼40. The collision vertices within a bunch crossing have an RMS spread of 180-200 ps in time. If the beam spot were to be sliced into consecutive snap shots of 30-40 ps then the pileup levels per snapshot would be approximately 40. The space-time reconstruction of a 200 pileup event is shown in Figure **??**. The addition of timing information to the z position spreads apart the vertices that would otherwise have been merged together and indiscernible. In order to achieve this a detector dedicated to the precise timing of minimum ionizing particles (MIPs), the MTD, will be added to the CMS detector.

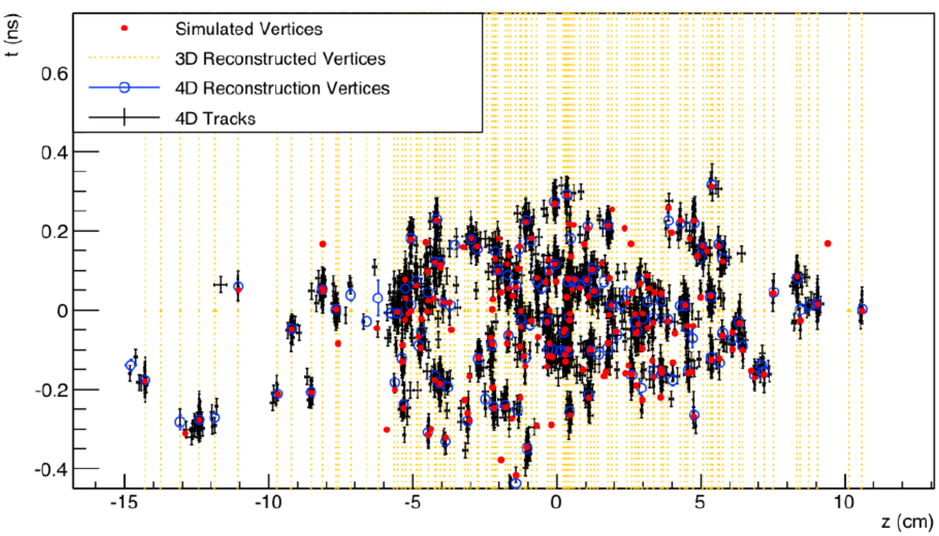

Fig. 5.2: Vertices from a simulated 200 pileup event with MTD timing resolution of ∼30 ps. The red dots represent the simulated vertices while the yellow lines indicate vertices reconstructed without the use of timing information. The black crosses and blue open circles represent tracks and vertices reconstructed using time information from the MTD. Reprint from

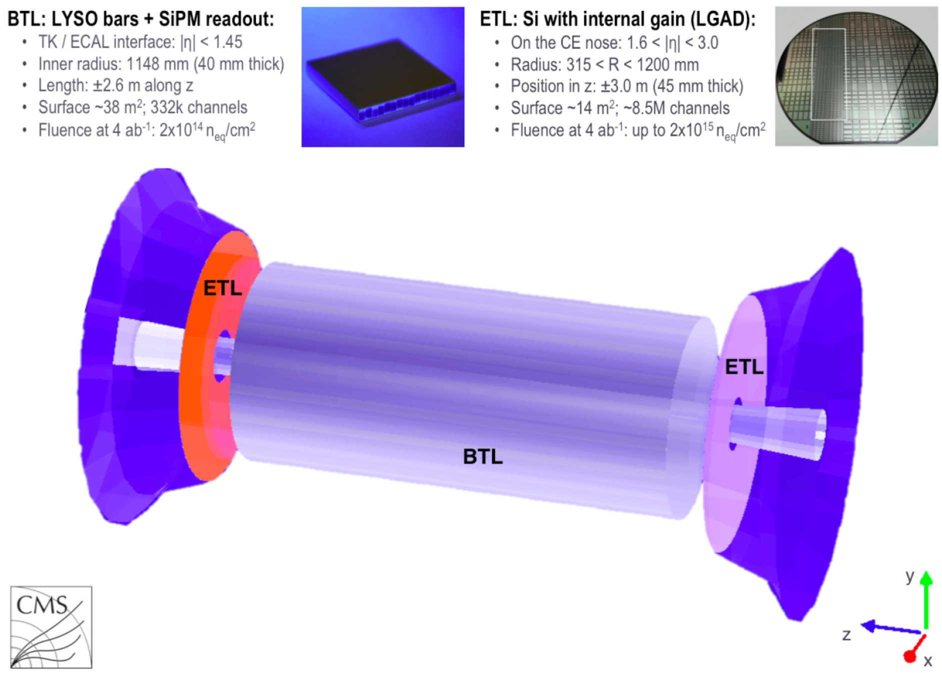

Fig. 5.3: Schematic view of the proposed MTD implemented in the GEANT simulation of the CMS detector. The central region makes up the BTL which will be located in the space between the tracker and the ECAL. The ETL will be located in front of the endcap calorimeter. Reprint from

5.2 Barrel Timing Layer

The Barrel Timing Layer (BTL) makes up the barrel region of the MTD. It will provide pseudorapidity coverage up to $|\eta| = 1.48$ with a geometric acceptance of $\sim 90\%$. The BTL will be capable of detecting MIPs with a time resolution of 30 ps at the start of Phase-2 operations and a luminosity-weighted time resolution of ~ 45 ps when radiation damage effects are taken into account.

The fundamental element for MIP detection in the BTL is a thin scintillating bar made of Lutetium Yttrium Orthosilicate crystals doped with Cerium ($(Lu_{1-X}Y_X)_2SiO_5 : Ce$) which is referred to as LYSO:Ce. The bars are 57 mm long, 3.12 mm wide, and have an average thickness of 3 mm. A silicon photomultiplier (SiPM) is attached to each end of the LYSO:Ce bar. This double-ended readout gives uniform time response along the length of the crystal by eliminating the time delay effect from light propagating along the crystal and the ability to extract positional information for tracking.

An overview of the BTL and its components is shown in Figure 5.4. The longitudinal axis of each crystal bar is oriented along the ϕ-direction in the CMS detector. The crystals are grouped in 1×16 ($\phi \times z$) arrays that each form a *module*. Each *module* has 32 SiPMs (2 for each bar) resulting in 32 readout channels. These *modules* are then grouped in a 3×8 ($\phi \times z$) arrangement to make up a readout unit (RU) as shown in Figure 5.5. Each *module* is read out by a dedicated ASIC called the TOFHIR (Time-of-flight, High Rate) chip which is capable of reading out 32 channels at a time. The TOFHIR chip gives precision timing information using discrimination of the leading edge of pulses from the SiPMs followed by a time-to-digital converter (TDC). When using discrimination techniques like this the time for a pulse to cross the discriminating threshold depends on the height of the pulse. This results in an amplitude-dependent timing variation called time walk. In order to correct for this time walk effect the ASIC also measures pulse amplitude. Six ASICs are mounted on each of four front-end boards (FEBs) on a RU giving a total of 24 ASICs and 768 SiPMs per RU. The RUs are then arranged in trays along the z-direction. Each tray holds six RUs, runs along half the length of the detector, and spans 10° along ϕ. To summarize, a total of 72 trays (36 azmuthal sections each split into a $+z$ and $-z$ section) contain 331776 SiPMs and 165888 LYSO:Ce bars. This gives a detector granularity that has an average occupancy of about 7% at 200 pileup, which limits the likelihood of multiple hits within a single crystal during a bunch crossing.

In order to have a negligible impact on the energy resolution of the ECAL, the thickness of the LYSO:Ce crystals is varied along the z-axis of the detector. This variation is done in three sections such that the thickness of material is as uniform as possible while not exceeding 0.4 X_0 where X_0 is one radiation length. This is done in three sections as a function of η

5.2.1 LYSO:Ce crystals

5.2.2 SiPMs

5.2.3 Glue qualification

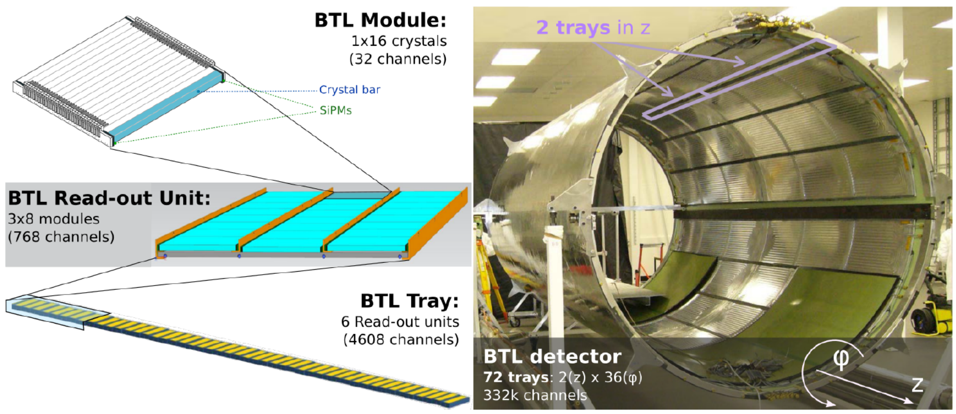

Fig. 5.4: On the left is an overview showing how the various components of the BTL fit together into modules, read-out units, and trays. On the right is a view of how the trays will fit into the Tracker Support Tube (TST)

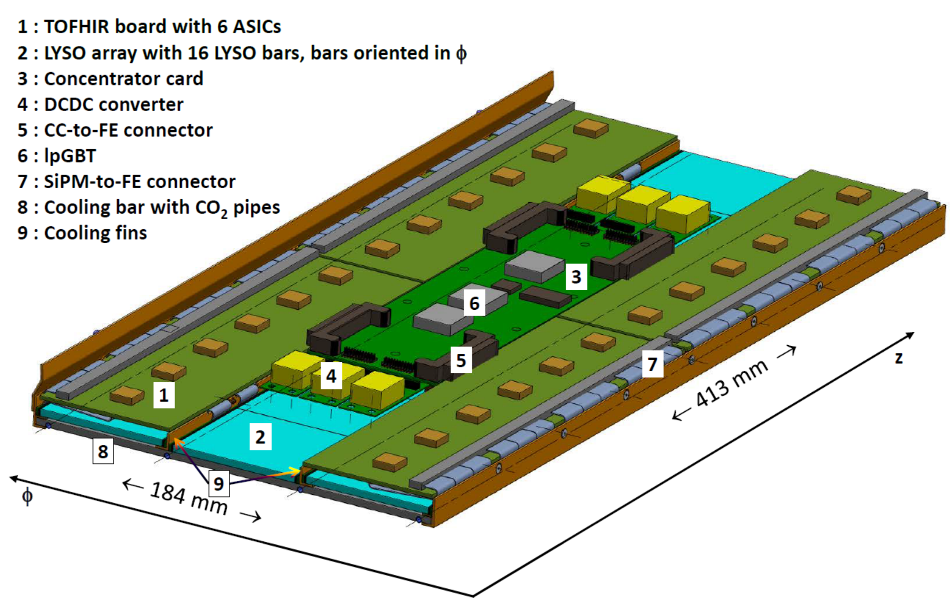

Fig. 5.5: Readout unit for the BTL.

6. CMS TRIGGER SYSTEM

When operating at nominal luminosity the LHC produces over 1 billion proton-proton collisions per second. Finite computing speed and storage capacity limit the rate at which CMS can record events to be about 1 kHz [9]. Decreasing the rate from 1 GHz to 1 kHz is accomplished by using a two-level trigger system to quickly decide which events will be discarded and which will be recorded. The first stage is a hardware-based Level 1 (L1) trigger and the second stage is software-based High Level Trigger (HLT).

6.1 L1 trigger

The L1 trigger decreases the rate by about six orders of magnitude from 1 GHz to 100 kHz by performing rough calculations on information from the ECAL, HCAL, and muon subsystems using field-programmable gate arrays (FPGAs). The L1 trigger can be divided further into the calorimeter and muon triggers. The schematic of the L1 trigger system in Figure 6.1 shows both the calorimeter and muon triggers. The calorimeter trigger trigger uses information from the ECAL and HCAL subdetectors to construct photon, electron, and jet candidates in addition to quantities such as missing transverse momentum and total hadronic activity. The muon trigger uses information from all three muon subsystems to construct muon candidates. The outputs from the calorimeter and muon triggers goes into the Global Trigger (GT) which decides which events should be recorded and which are to be discarded [27].

6.1.1 Calorimeter trigger

Trigger Primitives (TP) are the raw inputs from the ECAL and HCAL for the calorimeter trigger. The TP, which contain information regarding the energy deposits in the calorimeters, are passed to the first layer of the calorimeter trigger. This first layer consists of several FPGA cards that receive data from several bunch crossings, but are each mapped to a section of the detector. This data is then passed on to the second layer in such a way

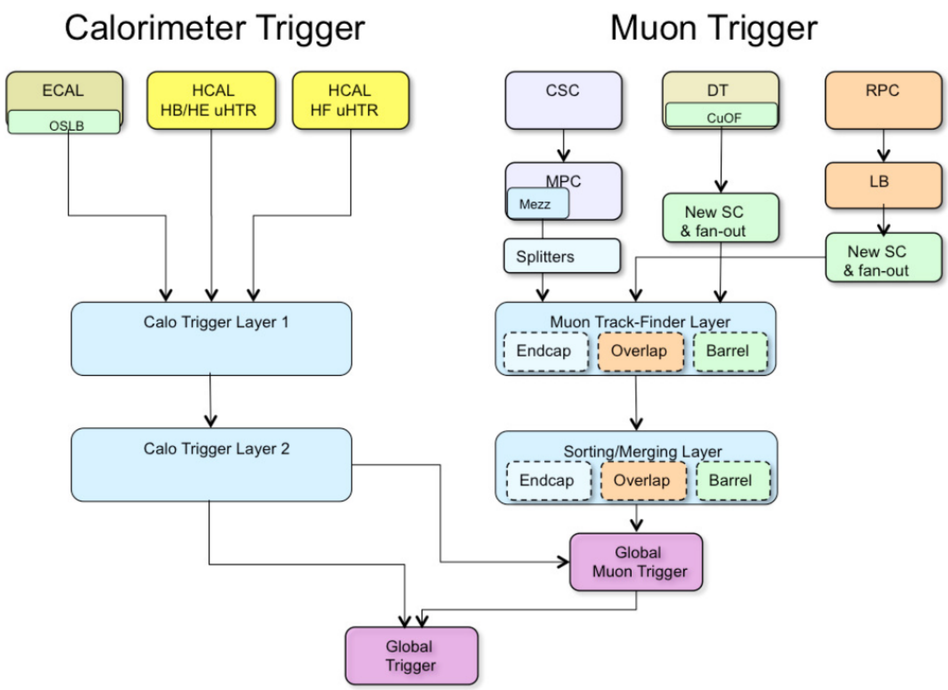

Fig. 6.1: L1 trigger system. Reprint from [3]

that each FPGA in this layer will receive data for the entire calorimeter for each bunch crossing. Candidate objects are then constructed and organized into a sorted list according to transverse momentum and passed on to the GT and the global muon trigger.

6.1.2 Muon trigger

TP for the muon trigger come from the three muon detectors, the CSCs, DTs, and RPCs. These are then passed on to the first layer of the muon trigger (Muon Track-Finding Layer) where the TP are combined to reconstruct muon tracks for sections of ϕ for different regions of $|\eta|$. The barrel track-finder for $|\eta| < 0.83$, the endcap track-finder for $|\eta| > 1.24$, and the overlap track-finder for $0.83 < |\eta| < 1.24$. This data is passed on to the second layer where the sections of ϕ are merged and subsequently passed on to the global muon trigger where it is combined with the output from Calo Trigger Layer 2 to compute isolation. The global muon trigger then combines the η regions and passes a list of the top eight muon candidates to the GT.

6.1.3 Global Trigger

Final processing of the reconstructed objects and quantities constructed by the calorimeter and muon triggers is carried out by the GT. L1 algorithms or ”seeds” are implemented by the GT using these objects. A full set of L1 seed is called a L1 menu and can be adjusted to meet the requirements of the CMS physics program. Each L1 seed can be given a ”prescale”, which is an integer value N that can be used to reduce the rate of a particular trigger path. This is done by only applying the trigger to one out of N events and can be used to take advantage of the current LHC running conditions.

6.2 High Level Trigger

Events that are accepted by the L1 trigger are passed on to the HLT which is based in software and is therefor capable of analyzing events with a higher degree of sophistication. The HLT has access to information from the full detector and implements ”paths” to select events of interest from those passing the L1 trigger. Each HLT path is a set of criteria that is used to either accept or reject an event. The full set of HLT paths is the HLT menu. Each HLT path is ”seeded” by one or more L1 seeds in order to decrease computing time. That means that a given HLT path will only be processed if the

L1 bits associated with its seed or seeds fire. Each HLT path is assigned to a primary dataset depending on its general physics signature. In the case of this analysis, the primary dataset used for signal events was DoubleEG for years 2016 and 2017. This was merged into the EGamma dataset for 2018. The SingleMuon dataset was used for trigger efficiency studies. A list of the primary HLT used for each year along with its associated primary dataset is listed in Table 6.1. The HLT path for 2016 is different because HLT_DoublePhoton70 was not a part of the HLT menu until 2017.

Tab. 6.1: Primary HLT

Year	HLT path	Primary dataset
2016	HLT_DoublePhoton60	DoubleEG
2017	HLT_DoublePhoton70	DoubleEG
2018	HLT_DoublePhoton70	EGamma

6.3 Trigger efficiency

7. CMS PARTICLE AND EVENT RECONSTRUCTION

After an event is chosen to be stored by the trigger system, the output from all of the sub-detectors is saved and recorded to disk as ”RAW” data. These data contain information about the response of each sub-detector, such as tracker hits and energy deposition in the calorimeters. As was mentioned in Chapter 4, shown in Table 4.1 and Figure 4.2, the CMS was designed such that each type of particle resulting from the *pp* collisions at the IP would leave a distinct signature in the sub-detectors. This allows for the information to be reconstructed into lists of physics object candidates such as photons, electrons, muons, etc and quantities such as missing transverse momentum. The particle flow (PF) algorithm performs this reconstruction by first building tracks and calorimeter clusters. These two elements are the inputs to the reconstruction of the aforementioned physics object candidates using a ”link” algorithm.

7.1 Tracks

A combinatorial track finder algorithm based on the Kalman filtering technique uses the hits in the silicon tracker to reconstruct tracks of charged particles [18]. Each iteration of the algorithm is comprised of three steps:

- Seed generation: Find a seed consisting of two to three hits that is compatible with a track from a charged particle.

- Track finding: Use pattern recognition to identify any hits that are compatible with the trajectory implied by the seed generated in the first step.

- Track fitting: Determine the properties of the track, such as origin, trajectory, and transverse momentum by performing a global χ^2 fit.

The first iteration uses stringent requirements on the seeds and the χ^2 of the track fit to pick out isolated jets which have very high purity. The hits associated with these high purity tracks are then removed to reduce the combinatorial complexity for subsequent iterations. This allows successive iterations to identify less obvious tracks by progressively loosening criteria while the removal of previously associated hits mitigates the likelihood of fake tracks being built.

7.2 Calorimeter clusters

Calorimeter clusters are constructed using energy deposition information from the calorimeters. Clusters are formed by first identifying the seed cell (ECAL crystal or HCAL scintillating tile) that corresponds to the local maxima of an energy deposit that is above a given threshold. Neighboring cells are then aggregated to grow topological clusters if their signals are above twice the standard deviation of the level of electronic noise.

7.3 Object identification

At this point the tracks and calorimeter clusters are linked to form a PF block. This linkage is done with an algorithm that quantifies the likelihood that a given track and cluster were results of the same particle. As PF blocks are identified as object candidates they are removed from the collection prior to each subsequent iteration until all tracks and clusters have been assigned to a PF object candidate. The following sections will outline how each of these PF objects is identified.

7.3.1 Muons

Muons are the easiest particle to identify, so they are the first objects reconstructed in the CMS. PF Muons are classified in three categories depending on how their tracks are reconstructed:

- Tracker muons: Tracks reconstructed from the inner tracker having $p_T > 0.5$ GeV and $|\vec{p}| > 2.5$ GeV that, when propagated to the muon system, match at least one hit in the muon chambers.
- Stand-alone muons: Tracks reconstructed only using hits in the muon system.
- Global muons: Stand-alone muons that coincide with a track from the inner tracker.

After a muon is reconstructed it is given an identification or ID based on observables such as the χ^2 of the track fit, how many hits were recorded per track, or how well the tracker and stand-alone tracks matched. These IDs represent different working points (loose, medium, and tight) which correspond to increasing purity but decreasing efficiency as you move from loose toward tight.

7.3.2 Electrons

The next objects reconstructed in the CMS are electrons. Bremsstrahlung in the tracker layers causes substantial energy loss and changes in momentum which requires the use of a dedicated tracking algorithm. In place of the Kalman filtering technique, a Gausian-sum filter (GSF) algorithm is used. This algorithm uses a weighted sum of Gaussian PDFs which does a better job of modeling the Bremsstrahlung effects than the Kalman filtering technique which uses a single Gaussian PDF.

PF ECAL clusters are regrouped by identifying a seed cluster then associating and adding clusters from Bremsstrahlung photons to form superclusters. The schematic in Figure 7.1 shows how the Bremsstrahlung photons are emitted in directions tangent to the trajectory of the electron. Electrons bending in the magnetic field causes spreading of PF ECAL clusters to typically occur along the ϕ-direction. Two approaches are used to associate the superclusters to GSF tracks. One is the ECAL-driven method, which uses superclusters with $p_T > 4$ GeV as seeds for the GSF track finding algorithm. This works well for high-p_T isolated electrons because the bend radius is less severe which decreases the spread of the PF ECAL clusters. This results in more of the Bremsstrahlung radiation being recovered and correctly assoiated with an electron candidate. The second approach is the tracker-driven method which uses tracks with $p_T > 2$ GeV as seeds that are propagated out to the surface of the ECAL and used for clustering. This method works best with soft electrons like those in jets because it relies on the high granularity of the tracker to disentangle overlapping energy deposits in the ECAL. [23]

As a final step, a boosted decision tree (BDT) is used to discriminate between real and fake electrons. The BDT is given variables associated with track-cluster matching, shower shape, and tracking. The output score of the BDT is used to classify electrons into loose, medium, and tight working points which exhibit to the same purity and efficiency trends as the muon working points.

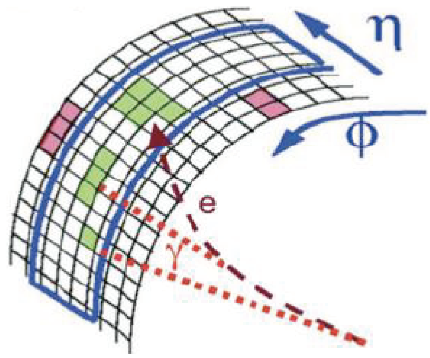

Fig. 7.1: The Bremsstrahlung photons continue along a straight trajectory while the electron path is bent by the magnetic field. This results in energy deposited in the calorimeter for such electrons to be spread out along the ϕ-direction.

7.3.3 Photons

Unlike electrons, photons typically deposit most of their energy in the ECAL without interacting with the tracker therefore their reconstruction is seeded from ECAL superclusters that do not have any GSF tracks associated with them. When photons interact with the tracker material they convert into electron-positron pairs which follow bent trajectories due to the magnetic field prior to entering the ECAL. This causes a spread of the energy deposition along the ϕ-direction. The goal of the clustering algorithm for photon reconstruction is to include all of the energy deposits of electrons resulting from photon conversions. As with the calorimeter clustering algorithm, the photon clustering starts by identifying a local energy maxima as a seed crystal. In the EB a cluster is made up of several parallel strips of crystals 5×1 in $\eta \times \phi$. The first strip has the seed crystal at its center. Neighboring strips in the ϕ-direction are added if they have energy above a threshold of 10 GeV but less than that of the subsequent strip with a maximum of 17 strips in a cluster. In the EE, the seed cluster is 5×5 with adjacent 5×5 clusters being added if they meet the minimum energy requirement.

Converted and unconverted photons can be differentiated by looking at how the energy is distributed in a supercluster. The variable R_9 is used for this purpose. It is defined as the ratio of the energy in a 3×3 crystal array to the energy in the entire supercluster. As the energy deposits resulting from converted electrons is more spread out they result in a lower R_9 value than unconverted photons. A photon is candidate is considered to be unconverted when $R_9 > 0.93$.

An important point regarding the clustering algorithm is that it does not differentiate between showers resulting from photons and those resulting from electrons. This allows for electron from $Z \to ee$ events to be used as high purity samples to study analysis inputs and for defining control regions using electron in place of photons.

7.3.4 Jets

When quarks or gluons are produced they hadronize to make cone-shaped, collimated collections of particles called jets. The jet clustering algorithm aims to combine these particles in order to accurately measure the kinematics of the initial gluon or quark. The algorithm uses the two distance parameters

$$d_{ij} = min(k_{T_i}^{2p}, k_{T_j}^{2p})\frac{\Delta R_{ij}^2}{R^2} \tag{7.1}$$

$$d_{iB} = k_{T_i}^{2p} \tag{7.2}$$

where d_{ij} is the distance between objects i and j and d_{iB} is the distance between object i and the beam B. The transverse momentum of the object is k_T. The parameter p is set either -1, 0, or +1 to specify whether the anti-k_T, inclusive Cambridge/Aachen, or inclusive k_T algorithm is used, respectively. The value of ΔR_{ij}^2 is defined as $(\eta_i - \eta_j)^2 + (\phi_i - \phi_j)^2$ and R is the distance parameter that defines the radius of the jet.

his analysis uses jets reconstructed from PF candidates using the anti-k_T algorithm with $R = 0.4$, also known as AK4PFJets or just PFJets. The algorithm goes through the following steps:

1. The smallest values of d_{ij} and d_{iB} are computed for all objects in the event.

2. Objects i and j are merged into a single object if $d_{ij} < d_{iB}$.

3. Object i is labeled as a jet and removed from the list if $d_{iB} < d_{ij}$.

Note for next time: Now talk about infrared and collinear safe. Use Allie's thesis for guide. Look at "recent thesis" for ECAL noise on 2017 data. Should also do JEC and JER in here.

7.4 Missing transverse momentum

8. DATA ANALYSIS

8.1 Overview

This analysis is motivated by the GGM supersymmetry breaking scenario in which the strong production of either gluinos or squarks result in a final state containing two photons, jets, and missing transverse momentum. Two example topologies are shown in Figure 8.1. If the T5gg model, each of the produced gluinos decays to a neutralino which then decays to a photon and a gravitino. Similarly, the T6gg model has each of the produced squarks decays to a neutralino which then decays to a photon and a gravitino. In both cases the gravitino escapes the CMS without detection which manifests as missing transverse momentum.

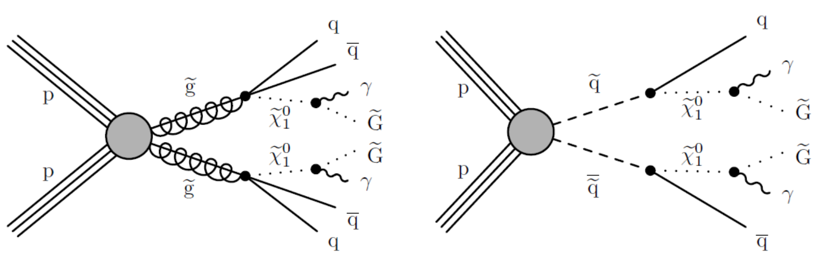

Fig. 8.1: Two examples of GGM supersymmetry breaking processes resulting in final states conaining two photons and missing transverse momentum. The T5gg model (left) shows gluinos produced from $p-p$ collisions which subsequently result in two neutralinos, each decaying to a photon and a gravitino. The T6gg model (right) shows squarks produced from $p-p$ collisions following a similar decay chain.

8.2 Data

This analysis was performed using 137 fb^{-1} of data collected from the CMS detector during the time period commonly referred to as Run 2 which spans from 2016 to 2018. The complete list of the datasets used can be found in

Table 8.1. The JSON files used to identify events passing all of the CMS offline data quality monitoring requirements are:

```
Cert_271036 284044_13TeV_23Sep2016ReReco_Collisions16_JSON.txt
Cert_294927 306462_13TeV_EOY2017ReReco_Collisions17_JSON_v1.txt
Cert_314472 325175_13TeV_PromptReco_Collisions18_JSON.txt
```

Tab. 8.1: Data Samples

/DoubleEG/Run2016B-17July2018-ver2-v1
/DoubleEG/Run2016C-17July2018-v1
/DoubleEG/Run2016D-17July2018-v1
/DoubleEG/Run2016E-17July2018-v1
/DoubleEG/Run2016F-17July2018-v1
/DoubleEG/Run2016G-17July2018-v1
/DoubleEG/Run2016H-17July2018-v1
/DoubleEG/Run2017B-31Mar2018-v1
/DoubleEG/Run2017C-31Mar2018-v1
/DoubleEG/Run2017D-31Mar2018-v1
/DoubleEG/Run2017E-31Mar2018-v1
/DoubleEG/Run2017F-31Mar2018-v1
/EGamma/Run2018A-17Sep2018-v2
/EGamma/Run2018B-17Sep2018-v1
/EGamma/Run2018C-17Sep2018-v1
/EGamma/Run2018D-22Jan2019-v2

8.3 Monte Carlo samples

Monte Carlo (MC) simulation were used to validate performance of the analysis on backgrounds, model background contributions, constructing a multivariate discriminant, and determining signal efficiencies.

8.4 Object definitions

The object candidates that are identified by the reconstruction algorithms are subject to further scrutiny in order to achieve optimal purities in the offline analysis.

8.4.1 Photons

Photons are required to have $p_T > 75$ GeV and meet the criteria prescribed by loose ID cuts derived by the e/γ Physics Object Group (EGM POG). The cut variables used to determine the photon ID are:

- H/E - The ratio of the energy deposited in the HCAL tower that is directly behind the ECAL supercluster associated with the photon to the energy deposited in the ECAL supercluster.
- $\sigma_{i\eta i\eta}$ - The log-fractional weighted width of a shower in $i\eta$-space. This variable is used to describe the shower shape.
- Particle Flow Charged Isolation - Sum of the p_T of charged hadrons associated with the primary vertex within a cone of $0.02 < \Delta R < 0.3$ of the supercluster.
- Particle Flow Neutral Isolation - Sum of the p_T of neutral hadrons associated with the primary vertex within a cone of $\Delta R < 0.3$ of the supercluster.
- Particle Flow Photon Isolation - Sum of the p_T of photons within a cone of $\Delta R < 0.3$ of the supercluster.

All of the isolation variables listed above are corrected in order to remove pileup. Table 8.2 gives a summary of the pileup-corrected requirements for a loose ID photon. The loose ID working point has an efficiency (background rejection) of 90.08% (86.25%) in the barrel and 90.65% (76.72%) in the end caps. In addition to the p_T and loose ID requirements, a photon must also pass a pixel seed veto (PSV). This means that there is no pixel seed matched to the photon.

Tab. 8.2: Summary of loose ID photons cuts

Variable	Cut Value (Barrel)	Cut Value (Endcap)
H/E	0.04596	0.0590
$\sigma_{i\eta i\eta}$	0.0106	0.0272
Charged Iso	1.694	2.089
Neutral Iso	$24.032 + 0.01512 p_{T\gamma} + 2.259 \times 10^{-5} p_{T\gamma}^2$	$19.722 + 0.0117 p_{T\gamma} + 2.3 \times 10^{-5} p_{T\gamma}^2$
Photon Iso	$2.876 + 0.004017 p_{T\gamma}$	$4.162 + 0.0037 p_{T\gamma}$

8.4.2 Electrons

As mentioned earlier, the clustering algorithm doesn't differentiate between showers from photons and those from electrons. In this analysis an electron is defined as an object that passes all of the photon requirements except for the PSV. Inverting the pixel seed requirement while using the same ID criteria insures that we have orthogonal selections while minimizing the bias potentially introduced by using control regions with electrons to model diphoton signal regions.

8.4.3 Muons

8.5 Backgrounds

The sources of background in this analysis can be grouped into three categories. In order of decreasing contribution they are mismeasured hadronic activity, electrons misidentified as photons, and standard model processes having final states with neutrinos and two photons. In events with multiple jets, limitations on the jet energy resolution can give rise to an apparent imbalance in p_T as is shown in Figure 8.2. Such events are usually from quantum chromodynamics (QCD) processes. In these cases jets can be misidentified as photons or there can be real photons being produced. In both cases the result is the appearance of two photons accompanied by E_T^{miss} which mimics our signal. Given the large cross-section for QCD, this is the most significant background in this analysis. The next background, resulting from the misidentification of electrons as photons, comes from electroweak (EWK) processes, in particular $W\gamma$ and $W + jets$ events where $W \rightarrow e\nu$. Here the neutrino contributes real E_T^{miss} while the fake photon allows this event to fulfill the diphoton requirement. The final background is from $Z\gamma\gamma \rightarrow \nu\nu\gamma\gamma$ events, which exactly mimic our signal, and is modeled using simulation as it is irreducible.

8.5.1 Instrumental background

The instrumental background is the contribution from events with spurious E_T^{miss} due to mismeasured hadronic activity. Since most of this background is comprised of QCD events, it is commonly referred to as the "QCD background" and those terms are used interchangeably in this thesis. Modeling of this background was done using the Rebalance and Smear technique while a multivariate discriminant was constructed to improve the efficiency of identifying events with fake E_T^{miss}.

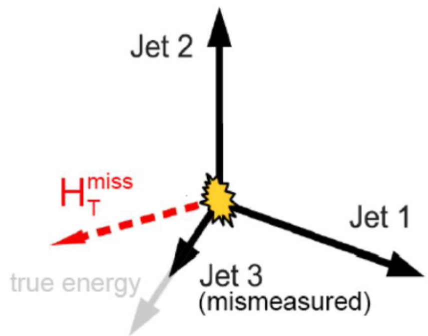

Fig. 8.2: Mismeasurement of Jet3 results in an inbalance in the events transverse momentum.

Rebalance and smear

The rebalance and smear method is used to model the spurious E_T^{miss} background. Coming soon....

Multivariate discriminant

A boosted decision tree (BDT) was used to develop a discriminating variable for identifying events with real E_T^{miss}. The variables used are listed below. All energy and momentum variables were normalized to the scalar sum of all of the p_T in the event $S_T = \sum_{\gamma, jets} |\vec{p}_{T_i}|$ in order to encourage the BDT to focus more on how the energy and momentum was distributed in an event rather than simply the scale of the energy or momentum.

- $S_{T_{jets}} = \sum_{jets} |\vec{p}_T|$
- $p_{T_{jets}} = \sum_{jets} \vec{p}_T$
- $p_{T_{\gamma\gamma}} = \vec{p}_{T_{\gamma_1}} + \vec{p}_{T_{\gamma_2}}$
- $HardE_T^{miss} = -\sum_i \vec{p}_{T_i}$
- $\Delta\Phi_{\gamma\gamma} = \Delta\Phi(\vec{p}_{T_{\gamma_1}}, \vec{p}_{T_{\gamma_2}})$
- $\Delta\Phi_{min} = min[\Delta\Phi(\vec{p}_{T_{HardE_T^{miss}}}, \vec{p}_{T_{jet_i}})]$
- $\Delta\Phi_1 = \Delta\Phi(\vec{p}_{T_{HardE_T^{miss}}}, \vec{p}_{T_{jet_1}})$

- $\Delta\Phi_2 = \Delta\Phi(\vec{p}_{T_{HardE_T^{miss}}}, \vec{p}_{T_{jet_2}})$
- $\Delta\Phi_{\gamma\gamma,HardE_T^{miss}} = \Delta\Phi(\vec{p}_{T_{HardE_T^{miss}}}, \vec{p}_{T_{\gamma\gamma}})$
- Add the delta R stuff...

8.5.2 Electroweak background

The electroweak background is dominated by events with $W \to e\nu$ where the electron is misidentified as a photon. Unlike the QCD background these events have real E_T^{miss} due to the presence of a neutrino. The key to estimating this background is determining the rate at which electrons get incorrectly labeled as photons in the signal region. This is done using a tag-and-probe method where the tag is an electron (a loose ID photon that fails the PSV) and the probe is categorized as either a photon or an electron. The result is an electron-electron region (ee) and an electron-photon region ($e\gamma$) that are selected from the data. As both of these regions contain $Z \to ee$ decays, fits are applied in each of the samples to the invariant mass spectra m_{ee} and $m_{e\gamma}$. The integrals of these fits are calculated over the range of the Z mass peak to give the number of events in each category.

8.5.3 Irreducible background

The irreducible $Z\gamma\gamma \to \nu\nu\gamma\gamma$ background produces two photons and has inherent E_T^{miss} via the neutrinos. There is no easy way to separate these events from our signal so it is estimated using MC simulation. The modeling of this background was tested using $Z\gamma\gamma \to \mu\mu\gamma\gamma$ and $Z\gamma\gamma \to ee\gamma\gamma$ events in data. Di-muon events with $|m_{\mu\mu} - m_Z| < 15$ GeV and di-electron events with $|m_{ee} - m_Z| < 15$ GeV were selected and the contribution of the muons/electrons was removed from the E_T^{miss} calculation to mimic $Z \to \nu\nu$. The event selection criteria for this $Z\gamma\gamma \to LL\gamma\gamma$ control region was

- HardMET > 100 GeV
- 2 looseID photons with $p_T > 30$ GeV
- 2 like-flavored leptons with $p_T > 30$ GeV

  2 mediumID muons or

  2 electons (looseID photons with a pixel seed).

The relationship

$$N_{Z\to\nu\nu} = \frac{b_{Z\to\nu\nu}}{b_{Z\to ee} + b_{Z\to\mu\mu}}(N_{Z\to ee} + N_{Z\to\mu\mu}) \tag{8.1}$$

gives an estimation for the number of $Z\gamma\gamma \to \nu\nu\gamma\gamma$ events expected given the number of $Z\gamma\gamma \to LL\gamma\gamma$ events observed in data where $N_{Z\to ee}$ and $N_{Z\to\mu\mu}$ are the number of data events passing the aforementioned selection criteria and $b_{Z\to\nu\nu}$, $b_{Z\to\mu\mu}$, and $b_{Z\to ee}$ are the branching ratios. The results are summarized in Table 8.3.

Tab. 8.3: Summary of $Z\gamma\gamma \to \nu\nu\gamma\gamma$ model validation

Year	Data-driven estimation	MC estimation	$\frac{data-driven}{MC}$
2016	30.2 +12.1 -9.0	33.8 ±0.31	0.893 +0.358 -0.267
2017	-	-	-
2018	-	-	-

BIBLIOGRAPHY

[1] *The CMS electromagnetic calorimeter project: Technical Design Report*. Technical design report. CMS. CERN, Geneva, 1997.

[2] *The CMS hadron calorimeter project: Technical Design Report*. Technical design report. CMS. CERN, Geneva, 1997.

[3] CMS Technical Design Report for the Level-1 Trigger Upgrade. 6 2013.

[4] S. Abdullin et al. The CMS barrel calorimeter response to particle beams from 2-GeV/c to 350-GeV/c. *Eur. Phys. J. C*, 60:359–373, 2009. [Erratum: Eur.Phys.J.C 61, 353–356 (2009)].

[5] L. Alvarez-Gaume and J. Ellis. Eyes on a prize particle. *Nature Phys*, 7:2–3, 2011.

[6] G. Apollinari, O. Brüning, T. Nakamoto, and Lucio Rossi. High Luminosity Large Hadron Collider HL-LHC. *CERN Yellow Rep.*, (5):1–19, 2015.

[7] S Baird. Accelerators for pedestrians; rev. version. Technical Report AB-Note-2007-014. CERN-AB-Note-2007-014. PS-OP-Note-95-17-Rev-2. CERN-PS-OP-Note-95-17-Rev-2, CERN, Geneva, Feb 2007.

[8] David Barney. CMS Slice. Feb 2015.

[9] L. Cadamuro. The CMS Level-1 trigger system for LHC Run II. *JINST*, 12(03):C03021, 2017.

[10] Jean-Luc Caron. Cross section of lhc dipole.. dipole lhc: coupe transversale. "AC Collection. Legacy of AC. Pictures from 1992 to 2002.", May 1998.

[11] S Chatrchyan et al. Precise Mapping of the Magnetic Field in the CMS Barrel Yoke using Cosmic Rays. *JINST*, 5:T03021, 2010.

[12] CMS Collaboration. CMS Technical Design Report for the Pixel Detector Upgrade. Technical Report CERN-LHCC-2012-016. CMS-TDR-11, Sep 2012. Additional contacts: Jeffrey Spalding, Fermilab, Jeffrey.Spalding@cern.ch Didier Contardo, Universite Claude Bernard-Lyon I, didier.claude.contardo@cern.ch.

[13] CMS Collaboration. Description and performance of track and primary-vertex reconstruction with the CMS tracker. *JINST*, 9(CMS-TRK-11-001. CERN-PH-EP-2014-070. CMS-TRK-11-001):P10009. 80 p, May 2014. Comments: Replaced with published version. Added journal reference and DOI.

[14] The CMS Collaboration. The CMS experiment at the CERN LHC. *Journal of Instrumentation*, 3(08):S08004–S08004, aug 2008.

[15] The CMS collaboration. The performance of the CMS muon detector in proton-proton collisions at √s=7 TeV at the LHC. *Journal of Instrumentation*, 8(11):P11002–P11002, nov 2013.

[16] Cinzia De Melis. Timeline for the LHC and High-Luminosity LHC. Frise chronologique du LHC et du LHC haute luminosité. Oct 2015. General Photo.

[17] Lyndon Evans and Philip Bryant. LHC machine. *Journal of Instrumentation*, 3(08):S08001–S08001, aug 2008.

[18] R. Fruhwirth. Application of Kalman filtering to track and vertex fitting. *Nucl. Instrum. Meth. A*, 262:444–450, 1987.

[19] Murray Gell-Mann. A Schematic Model of Baryons and Mesons. *Phys. Lett.*, 8:214–215, 1964.

[20] J. Goldstone. Field Theories with Superconductor Solutions. *Nuovo Cim.*, 19:154–164, 1961.

[21] Peter W. Higgs. Broken Symmetries and the Masses of Gauge Bosons. *Phys. Rev. Lett.*, 13:508–509, 1964.

[22] Yutaro Iiyama. *Search for Supersymmetry in pp Collisions at $\sqrt{s}$ = 8 TeV with a Photon, Lepton, and Missing Transverse Energy*. PhD thesis, Carnegie Mellon U., 2 2015.

[23] Jonas Rembser. CMS Electron and Photon Performance at 13 TeV. *J. Phys.: Conf. Ser.*, 1162(1):012008. 8 p, 2019.

[24] Tai Sakuma and Thomas McCauley. Detector and event visualization with SketchUp at the CMS experiment. *Journal of Physics: Conference Series*, 513(2):022032, jun 2014.

[25] A.M. Sirunyan et al. Performance of the CMS muon detector and muon reconstruction with proton-proton collisions at $\sqrt{s}$=13 TeV. *Journal of Instrumentation*, 13(06):P06015–P06015, jun 2018.

[26] Steven Weinberg. The Making of the standard model. *Eur. Phys. J. C*, 34:5–13, 2004.

[27] J. Wittmann, B. Arnold, H. Bergauer, M. Jeitler, T. Matsushita, D. Rabady, B. Rahbaran, and C.-E. Wulz. The upgrade of the CMS global trigger. *Journal of Instrumentation*, 11(02):C02029–C02029, feb 2016.

[28] Chen-Ning Yang and Robert L. Mills. Conservation of Isotopic Spin and Isotopic Gauge Invariance. *Phys. Rev.*, 96:191–195, 1954.

[29] G. Zweig. *An SU(3) model for strong interaction symmetry and its breaking. Version 2.* 2 1964.